FOREWORD

This report was prepared by the Internal Aerodynamics Group of the Aeromechanics Section, Air Force Flight Dynamics Laboratory under Task 136605 "Hypersonic Induction System Research" on Project 1366 "Aerodynamics and Flight Mechanics." This Task and Project are a part of Air Force System Command's Applied Research Program 750A, "Mechanics of Flight."

This study was conducted by Mr. Paul H. Kutschenreuter Jr., Task Engineer, Mr. Richard L. Balent and Mr. George K. Richey. The authors wish to thank the other engineers of the Internal Aerodynamics Group for their contributions to this effort.

ABSTRACT

Two hypersonic inlet models were designed for force balance testing in the Cornell Aeronautical Laboratory 48-inch shock tunnel over a Mach Number range of 8 to 16. The performance of these models is to be established experimentally on the basis of their measured internal drag. Reasons for considering this method of establishing hypersonic inlet performance and use of the associated "drag equivalent" pressure recovery are discussed. The design of these models, the resulting inlet geometry, and the related performance calculations are described.

This technical documentary report has been reviewed and is approved.

Philip P Antonatos

PHILIP P. ANTONATOS
Chief, Flight Mechanics Division
AF Flight Dynamics Laboratory

TABLE OF CONTENTS

ILLUSTRATIONS

SYMBOLS

A	- area
C_{D_f}	- friction drag coefficient
C_{D_i}	- internal drag coefficient
D_i	- internal drag
F_N	- net thrust
F/A	- fuel to air ratio
g	- gravitational constant
H	- total pressure
h	- static enthalpy
I_{sp}	- specific impulse
K	- stream function parameter
l	- longitudinal distance
M	- mach number
P	- static pressure
q	- dynamic pressure
Re/l	- unit Reynolds number/ft
T	- static temperature
u	- local velocity for non-uniform flow
v	- velocity for uniform or reference flow
z	$= \rho_2 V_2^2 y_2 \left(1 - \frac{\theta}{y_2} - \frac{\delta^*}{y_2}\right)$
β_i	- mach angle
δ	- boundary layer thickness
δ^*	- boundary layer displacement thickness
η	- pressure recovery

θ - boundary layer momentum thickness

θ_i - flow angle

ρ - density

SUBSCRIPTS

$_0$ - free stream conditions

$_2$ - diffuser exit conditions

$_\ell$ - local conditions

$_{MOA}$ - momentum weighted average conditions

$_{MW}$ - mass weighted average conditions

INTRODUCTION

Inlet performance estimation for supersonic burning ramjets presents many new problems compared to established procedures used in conjunction with the more conventional subsonic burning ramjet. Early engine performance estimates are usually based on the results of one-dimensional cycle calculations (Reference 1). Initially, levels of component efficiency are assumed for major components such as the inlet, combustor, and nozzle. Experimental programs are usually initiated to determine and to demonstrate levels of component efficiency for particular configurations. Often, such experimentally determined component efficiencies are used to refine the original cycle calculations to provide estimates of expected performance for a complete engine. The adequacy of this procedure must, among other things, depend upon the degree of consistency between the actual experimental performance of the component in question, and the one-dimensional efficiency parameter used to represent it in the cycle analysis. Basically, to establish engine net thrust from component performance data, it is to be expected that the one-dimensional efficiency parameters utilized, should represent the correct change in the internal total momentum of the fluid flow through each component.

For hypersonic inlet performance, it is noted that most experimental data taken in ground test facilities indicate that the supersonic and hypersonic duct flow profiles are generally far from uniform due to viscous effects and shock interactions (References 2 and 3). Consequently, some method of "averaging" must be employed to provide the required one-dimensional input for cycle calculations. In subsonic burning ramjets, these non-uniform supersonic flow profiles upstream of the inlet throat are afforded an opportunity to mix to a more uniform flow in the subsonic diffuser. In addition, the increasing flow area of the subsonic diffuser permits the attainment of relatively low values of boundary layer thickness to duct passage height compared to supersonic conditions upstream of the inlet throat, and because of the relatively low subsonic exit Mach Number, the velocity difference across the boundary layer is significantly reduced. The effects of these latter two phenomena are to increase the degree with which the subsonic non-uniform exit flow profile can be adequately represented by various one-dimensional averaging techniques. In contrast, for supersonic burning ramjets the exit flow profile is not afforded this mixing opportunity in the inlet, and the ratio of boundary layer thickness to passage height may be large, necessitating the use of some appropriate "averaging" technique.

Two such common methods of "averaging" a non-uniform property (Figure 1) such as H(y), the inlet total pressure, are:

$$\text{MASS WEIGHTED AVERAGE: } \bar{H}_{MW} \equiv \frac{1}{\rho_0 V_0 A_0} \int_0^{A_2} H \rho \, u \, dA$$

$$\text{MOMENTUM WEIGHTED AVERAGE: } \bar{H}_{MOA} \equiv \frac{1}{Z} \int_0^{A_2} H \rho \, u^2 \, dA$$

Manuscript released by the authors, December 1963, for publication as an FDL Technical Documentary Report.

If the existence of a finite "core" flow (Figure 1) is assumed, it can readily be shown for constant static pressure across a two-dimensional duct at the exit station, that:

$$(\overline{\eta}_R)_{MW} = \frac{H_2}{H_0}\left[\frac{(1-\frac{\delta}{y_2})}{(1-\frac{\delta^*}{y_2})} + \frac{1}{(1-\frac{\delta^*}{y_2})}\int_0^{\delta/y_2}\frac{H}{H_2}\frac{\rho u}{\rho_2 V_2}\frac{dy}{y_2}\right] \tag{1}$$

$$(\overline{\eta}_R)_{MW} \approx \frac{H_2}{H_0}\frac{(1-\frac{\delta}{y_2})}{\left[1-\frac{\delta}{y_2}(\frac{\delta^*}{\delta})\right]} \tag{2}$$

$$(\overline{\eta}_R)_{MOA} = \frac{1}{M}\frac{H_2}{H_0}\left[\rho_2 V_2^2 (y_2-\delta) + \int_0^{\delta}\frac{H}{H_2}\rho u^2 dy\right] \tag{3}$$

$$(\overline{\eta}_R)_{MOA} \approx \frac{H_2}{H_0}\frac{(1-\frac{\delta}{y_2})}{\left[1-\frac{\delta}{y_2}(\frac{\theta}{\delta}+\frac{\delta^*}{\delta})\right]} \tag{4}$$

Equations 2 and 4, show that $(\overline{\eta}_R)_{MW}$ is slightly less than $(\overline{\eta}_R)_{MOA}$ since θ is generally much less than δ^*. An appreciation of the effect that mass averaging has on "core" flow pressure recovery can be obtained from Figure 2. It is concluded from this figure that for hypersonic inlets with values of $\frac{\delta}{y_2}$ greater than about .25, significant deviations from "core" flow values of inlet pressure recovery occur in spite of the fact that, per unit height, there is less mass flow and momentum in the boundary layer compared to that in the "core" flow.

More important, however, is the degree of representation of the actual change in the internal total momentum during the inlet compression process, afforded by the use of such "averaged" one-dimensional efficiency parameters. To explore this point, it is instructive to examine several different methods of averaging the pressure recovery for specific non-uniform exit flow profiles, and then to determine the extent to which such averaging techniques account for the actual change in internal total momentum (drag) of the fluid flow through the inlet.

Consider then, the simplified analytical model of Figure 3. For purposes of this analysis, the inlet lines between stations 0 and 2 are unimportant. Basic considerations require only that the continuity and momentum equations be satisfied between these two stations. (For this example the flow is assumed to be adiabatic.) Using standard boundary layer integral parameter notation, the continuity equation can be written as:

$$\frac{\delta}{y_2} = \frac{1-\frac{y_0}{y_2}\left(\frac{T_0}{T_2}\right)^3\frac{M_0}{M_2}\frac{H_0}{H_2}}{(\frac{\delta^*}{\delta})} \tag{5}$$

Similarly, the momentum equation is:

$$C_{D_i} = 2\left[1 - \frac{q_2}{q_0}\frac{y_2}{y_0}\left\{1 - \frac{\delta}{y_2}\left(\frac{\delta^*}{\delta} + \frac{\theta}{\delta}\right)\right\}\right] - \frac{y_2}{y_0}\frac{P_0}{q_0}\left(\frac{P_2}{P_0} - 1\right) \qquad (6)$$

By selecting values for M_0 and $\frac{y_0}{y_2}$, and then maintaining a particular value of "core" flow pressure recovery $\frac{H_2}{H_0}$, it is possible to systematically vary $\frac{\delta}{y_2}$ for different values of boundary layer power law profiles and to compute the corresponding change in the internal total momentum (internal drag coefficient,) using Equations 5 and 6. Results of such calculations are presented in Figure 4 using Equation 2 to obtain a one-dimensional average of the resulting non-uniform profiles for "core" flow pressure recoveries of 1.00, 50 and .25 as indicated. The other curve of this figure is the complete inviscid uniform flow solution. Figure 4 is repeated in Figure 5 with lines of corresponding $\frac{\delta}{y_2}$ superimposed. With the aid of Figure 6 the object comparison can now be made. It is immediately observed that for the same measured level of internal drag coefficient, (point (1) in Figure 6, obtainable either from flow profile integration or direct force measurement) the mass weighted one-dimensional pressure recovery is always greater than the one-dimensional pressure recovery of the inviscid uniform flow solution. More significant, however, is the fact that use of the "drag-equivalent" pressure recovery as defined by the inviscid uniform flow solution, in conjunction with the physical inlet geometric contraction ratio must by its very definition, permit calculation of the actual change in internal momentum or internal drag of the inlet. On the other hand, use of the one-dimensional mass weighted value of inlet pressure recovery for cycle calculation purposes in conjunction with the physical inlet geometric contraction ratio can result in a significant underestimation of the actual change in internal momentum (point (2) in Figure 6). The use of "core" flow pressure recovery results in a further misrepresentation of the internal drag coefficient, essentially ignoring viscous effects completely. Although this situation could be remedied somewhat by use of an "effective" flow area rather than the actual geometrical flow area (when values of "core" flow and mass weighted pressure recovery from experimental data are used in one-dimensional engine cycle calculations) the chances are that if only "core" flow measurements can be taken, or at best, the mass weighted pressure recovery approximated, then the required "effective" flow area cannot be adequately determined.

Proceeding on this assumption, it must next be determined to what degree such inconsistencies in the internal drag coefficient may influence cycle calculated net thrust. Limiting such considerations to only that difference in the inlet drag inferred by the use of "core" flow and mass weighted values of inlet pressure recovery instead of the correct "drag equivalent" pressure recovery, Figure 7 is directly obtainable from Figures 4 and 5 and the assumption of nominal values of I_{sp} since:

$$\frac{D_i}{F_N} = \frac{V_0}{2g}\frac{C_{D_i}}{(F/A)\,I_{sp}} \qquad (7)$$

and:

$$\frac{\Delta F_N}{F_N} = \frac{V_0}{2g}\left[\frac{C_{D_{i\,ACTUAL}}}{(F/A)\,I_{sp}}\right]\frac{\Delta C_{D_i}}{C_{D_{i\,ACTUAL}}} \qquad (8)$$

Since the values of I_{sp} used in the preparation of Figure 7 are based on the calculations of Reference 4 which utilizes a rather idealized cycle analysis, the resulting values of $\frac{\Delta F_N}{F_N}$ are considered to be conservative for the conditions indicated. This figure shows that significant overestimations of cycle net thrust can occur for inlet boundary layer thickness ratios representative of current experimental data. Although such boundary layer thickness ratios may be somewhat exaggerated due to comparatively low Unit Reynold's number testing and small-scale models compared to flight conditions, it must be remembered that it is from such tests that component efficiencies are often established for use in engine cycle calculations. Various boundary layer control techniques may be employed to obtain lower values of $\frac{\delta}{y_2}$ and thus promote more uniform profiles at the diffuser exit, but a proper "bookkeeping" system that accounts for all of the inlet airflow must, of course, eventually charge the inlet for its skin friction drag. Even without specific knowledge as to the extent of such boundary layer control techniques, and with instrumentation only adequate enough for "core" flow pressure recovery determination and inlet longitudinal static pressure distribution, an approximation to the "drag-equivalent" pressure recovery can still be made based on direct skin friction estimates.

As an example, consider the simple compression system illustrated in Figure 8. Using the Eckert Reference Temperature Method in conjunction with the Blasius flat plate skin friction law and the Sutherland viscosity relationship the following expression is obtained:

$$C_{D_f} = \frac{.664\left(\frac{H_2}{H_0}\right)^{-.0715}}{\sqrt{\frac{R_{e_0}}{\ell}\cdot h_0}} \int_0^{\ell/h_0} \frac{\left(\frac{P_\ell}{P_0}\right)^{.5715}\left\{\left(\frac{P_0}{P_\ell}\right)^{.286}\left(\frac{H_2}{H_0}\right)^{.286}\left[.5\frac{T_w}{T_0}+.22\left(\frac{H_0}{P_0}\right)^{.286}\right]+.28\right\}^{\frac{1}{4}}}{\sqrt{\frac{.5\frac{T_w}{T_0}+.22\left(\frac{H_0}{P_0}\right)^{.286}+.28\left(\frac{P_\ell}{P_0}\right)^{.286}\left(\frac{H_0}{H_2}\right)^{.286}+\frac{199}{T_0}}{1+\frac{199}{T_0}}}} \frac{d\,\ell/h_0}{\sqrt{\ell/h_0}} \qquad (9)$$

Evaluating (Equation 9) at the conditions indicated on Figure 8 for a theoretical static pressure distribution culminating in a static pressure ratio of 300 with a "core" flow pressure recovery of .50, an estimated friction drag coefficient for the upper and lower compression surfaces of 0.03 is obtained, assuming the flow remains laminar all the way to the exit station. As shown in the lower portion of Figure 8, the "drag-equivalent" pressure recovery is approximately 0.380 and the actual internal drag coefficient is approximately 18 percent greater than the value "inferred" from the "core" flow pressure recovery.

Through these simple examples, the desirability of some technique such as the "drag-equivalent" pressure recovery to define the change in total momentum of the inlet airflow for purposes of either engine cycle analysis or comparison of the performance of different inlets, is evident. Experimentally, this can be accomplished by either direct force measurement or from detailed integration of measured pitot pressure profiles. The latter more conventional method of flow profile measurement becomes difficult to apply to models with relatively small exit-duct passages and three-dimensional inlet configurations with duct exits of unusual cross section. The "paper" feasibility of using a force balance system to measure inlet internal drag directly and then back-calculate what is now called the "drag-equivalent" pressure recovery was reported earlier in Reference 5, and more recently in greater detail in Reference 6. For the purpose of evaluating the experimental practicality

of such a method, and simultaneously to obtain required inlet performance data, two basic inlet models were designed by the Internal Aerodynamics Group of the Aeromechanics Branch, Air Force Flight Dynamics Laboratory. The Cornell Aeronautical Laboratory, under Air Force Contract AF 33(657)-11414, was awarded the responsibility of fabricating, instrumenting and testing these designs in the CAL 48-inch shock tunnel, over a Mach number range from 8 to 16. This report describes the aerodynamic design of these models, the resulting inlet geometry, and the associated performance calculations.

AERODYNAMIC CONFIGURATION SELECTION AND DESIGN APPROACH

Although the inlet models designed for evaluating the proposed force balance internal drag measurement technique had to be specifically tailored for that purpose, consideration was also given to the simulation of particular full-scale design characteristics. In addition, it was decided that the configurations tested should be amenable to reasonable theoretical analysis in order to provide the additional opportunity of checking the adequacy of inlet performance estimation techniques.

The basic configuration determined to be most suitable for meeting the above requirements was an axisymmetric, external-internal compression inlet with an "X"-wave shock supported by intermediate isentropic compression (Figure 1). A design point Mach number of 16 was selected at a Unit Reynold's number of 10^5. Design point calculations at these shock tunnel conditions were made assuming the boundary layer was laminar and attached. The inlet wall contours were corrected for the laminar boundary layer growth by means of an iterative, combination Method of Characteristics solution of the "effective" body comprised of the actual wall contour, and the laminar boundary layer displacement thickness. The actual wall contour was continually modified until the iterated "effective" body had the desired characteristics solution for the inviscid flow.

To provide a configuration with a more favorable wetted area distribution and one with cowl spillage area for "starting" purposes, a second cowl was designed. This "swept-lip" configuration was evolved from the basic axisymmetric solution by tracing streamlines originating at the intersection of the axisymmetric cowl shock and a selected "cutting" plane (Figure 9). The laminar boundary layer growth associated with these swept-lip cowl streamlines was then estimated and substracted to determine the actual cowl contours.

Since inlet losses, aerodynamic heating, and duct loads all increase with the amount of flow compression, it was decided to design these inlets for a minimum amount of compression at the design Mach number. In consideration of full-scale simulation, this minimum amount of compression was defined to be that for which auto-ignition of hydrogen would occur in the atmosphere. Assuming this temperature to be 2000° R, for most flight trajectories this would require a minimum static temperature ratio of about 5. This temperature ratio was selected as the target compression index for design point shock tunnel testing.

Experimental considerations dictated that the internal duct contours be designed so that positive drag loads always act on both the centerbody and the cowl. Otherwise, accurate measurement of small component forces becomes a difficult problem for a single force balance system which must also be capable of accurately measuring much larger loads at other test conditions. For this reason, the internal duct lines were designed to achieve stream aligned flow at the exit.

To provide experimental flexibility, provision was made for fore and aft spike translation, but at a constant value of inlet geometric contraction ratio. Only minor changes in the flow field are sought from the spike translation and the exit area is maintained constant to facilitate data reduction. The equations used to back-calculate the "drag-equivalent" pressure recovery can be expanded to provide an indirect assessment of the over-all boundary layer development (Reference 6), if constant static pressure is maintained across the duct at the exit station, and the value of this pressure rise is known. (With variable throat area when the spike is translated, it is difficult to maintain a compression balance between the contributions of the spike and the cowl, and hence constant static pressure across the duct exit.) The aft portion of the constant area duct was instrumented with static pressure transducers to provide direct indication of the degree of actual compression achieved, and to provide an indication of the static pressure variation across the constant area duct.

The above outlined design approach was "dry-run" in a simpler version to demonstrate its feasibility and to permit identification of possible problem areas. The results of this study are reported in Reference 7 and a mock-up of the inlet designed as a result of that study is shown in Figure 10. This full-scale model proved to be a valuable visual aid in arriving at the final aerodynamic lines of the swept-lip cowl configuration.

AERODYNAMIC DESIGN PROCEDURES EMPLOYED

Preliminary studies indicated that the selected degree of compression could be achieved with a reasonable degree of efficiency at Mach 16 with a two shock, "X"-wave system supported with intermediate isentropic compression as indicated in Figure 1. Ideally, the incident shocks would be cancelled at points A and B to provide uniform flow at a compression temperature ratio of approximately 5. Nonfocused isentropic compression was selected to minimize the wall pressure gradients associated with the resulting wall pressure rise. Although firm boundary layer separation criteria has yet to be established for hypersonic laminar shock-boundary layer interactions, the curves of Figure 11 were used to assess the probability of laminar separation for the design of these models. The required inlet oblique shock pressure rise is in excess of the separation plateau pressure ratios indicated by the curves of Figure 11. This does not necessarily indicate separation, however, since data indicate (Reference 8) that for "mild" laminar separation, the separation-plateau pressure rise is always less than the final pressure rise. (For mild separation, although a definite separation plateau appears in the wall pressure distribution, the design pressure rise is still achieved in a relatively short distance downstream of the plateau region.)

Based on preliminary one-dimensional calculations, it was determined that the target compression could be efficiently achieved with an "X"-wave shock system made up of 5 degrees turning through the initial shock, 5 degrees isentropic turning and then 5 degrees turning back to the stream direction through the incident shock, followed by 5 more degrees of isentropic turning to bring the flow back to the free-stream direction. At Mach 16 this would require a shock wave angle of about 8 degrees. Due to shock curvature resulting from viscous effects, it was necessary to find a centerbody and cowl that would generate an 8-degree asymptotic shock for the Mach 16 shock tunnel conditions. By "chaining" together an existing laminar boundary layer analysis (Reference 9) based on the method of Reference 10, and a previously written axisymmetric rotational Method of Characteristics program, (Reference 11), it was possible to iterate between the inviscid and viscid flow fields to establish a compatible solution. Using this method, an initial characteristics solution is established for the original "physical" wall coordinates which are input as a polynomial curve fit. (The machine automatically selects the best curve fit, up to a polynomial of degree 20.) The output of the characteristics solution is then automatically fed into the boundary layer program and the calculated boundary layer displacement thickness is added to the "physical" wall coordinates. This new effective body is curve-fit, and the procedure automatically repeated for the selected number of iterations. Computational results for 3 and 4 iterations are presented in Figures 12 and 13 respectively for a 5.75-degree half angle cone at Mach 16. This technique was checked out using Schlieren data from References 3 and 12 as a basis for validation. The agreement between the calculated shock shape and that discernible from the Schlieren pictures is shown in Reference 11 to be excellent. Similar agreement between the calculated boundary layer displacement thickness and that indicated by the Schlieren is shown in Reference 9.

The computed results of Figure 13 clearly indicate a lag in the attainment of the inviscid pressure rise. This has also been noted in experimental data from different sources (References 3 and 13) and is attributed to thinning of the boundary layer in the adverse pressure gradient region. Such thinning apparently results in lower effective flow angles at the edge of the "effective" body, compared to greater inclination angles of the "physical" wall, until the boundary layer growth becomes influenced more by wall shearing forces than by stream compression.

The axisymmetric cowl flow field was established by a somewhat different procedure. The relatively low Unit Reynold's number, and increased boundary layer growth rate for the cowl surface as compared to the cone, increase the effective bluntness of the leading edge. In an attempt to maintain desired accuracy in the Method of Characteristics calculations without going to a blunt body solution at the leading edge, use was made of the General Electric Bertram boundary layer program (Reference 14). This program, which iterates the boundary layer solution as calculations proceed downstream, was used to obtain the iterated boundary layer solution in the vicinity of the cowl leading edge, upstream of the compression region. The resulting boundary layer displacement thickness was then "faired" on through the compression turn until the characteristics solution of such an "effective" body indicated that the desired inviscid compression system had been established. From this "effective" cowl contour, the boundary layer displacement thickness was subtracted. For the region downstream of the leading edge an approximate technique was devised to estimate δ^*, based on the method of Reference 10. This method is based on the assumption that the boundary layer growth rate in a region of adverse pressure gradient is governed by an increase in δ^* due to viscous shear and a decrease in δ^* based on stream tube compression. It was further assumed that these two effects can be linearly combined and that the local "shear" growth rate can be calculated using zero pressure gradient results of Reference 10, and that the compression "thinning" can be calculated by considering the

"isentropic" compression of the boundary layer flow. A comparison of this approximate technique in an adverse pressure gradient region with the standard Cohen-Reshotko method substantiated the adequacy of the devised technique at the conditions employed.

The effective surface Mach number distribution for the axisymmetric cowl is presented in Figure 14. As indicated, the favorable pressure gradient associated with the leading edge viscous interaction extends downstream for several inches, delaying the initiation of the wall compression process. The small over-expansion hump in this curve is apparently caused by the curve-fit used to represent the effective body surface. It was noted that the use of the higher degree polynomials for this purpose, while permitting a better overall representation of the surface, did often result in a mild degree of wall waviness, the effects of which will show up in a tight characteristics mesh.

In order to extend both the viscous and inviscid calculations downstream of the impinging oblique shocks, an approximation had to be devised. Although in actuality the shock pressure rise through the boundary layer along the wall is not a discontinuity as in the inviscid case, the propagated pressure distribution upstream and downstream of the shock impingement point cannot be represented adequately enough to justify the use of conventional continuous pressure gradient calculation procedures. It was elected instead, to devise a rather simple approach in which it was assumed that at a short distance upstream and downstream of the shock impingement point the boundary layer profiles were similar. The local entropy increase through the shock was taken into account to establish the inviscid conditions at the edge of the downstream boundary layer profile. By further assuming that the mass flow in the boundary layer remains constant between these stations upstream and downstream of the shock impingement point, the displacement thickness ratio can be computed from:

$$\frac{\delta_2^*}{\delta_1^*} = \left(\frac{\delta_2}{\delta_1}\right) \frac{\left[\int_0^1 \left(1 - \frac{u/V}{T/T_T}\right)_1 dy/\delta\right]}{\left[\int_0^1 \left(1 - \frac{u/V}{T/T_T}\right)_2 dy/\delta\right]} \tag{10}$$

where:

$$\frac{\delta_2}{\delta_1} = \frac{P_1}{P_2}\,\frac{M_1}{M_2}\,\sqrt{\frac{T_2}{T_1}} \left[\frac{1 - \int_0^1 \left(1 - \frac{u/V}{T/T_T}\right)_1 dy/\delta}{1 - \int_0^1 \left(1 - \frac{u/V}{T/T_T}\right)_2 dy/\delta}\right] \tag{11}$$

Results of such calculations for a linear velocity profile are presented in Figures 15 and 16: (The thinning trend predicted by this simple analysis is substantiated experimentally by the shock-boundary layer impingement Schlierens of Reference 3.) The "physical" wall angles in the vicinity of the shock impingement point were contoured in an attempt to avoid large local expansions in the event the shock structure deviated significantly from that calculated. Although such local expansions may prove to be beneficial in weakening the strength of the impinging shock, and lessening the chances of boundary layer separation, such a practice can lead to "false economy" since the entropy price has been paid once for the diffusion achieved upstream of the impinging shock, and no "refund" is given when the flow is expanded.

The downstream half of the "X"-wave shock structure was calculated using a specially written axisymmetric rotational Method of Characteristics program for the CDC 160A computer, incorporating established calculation routines from the "parent" 7094 program of Reference 11. By using the 160A computer, the development of the flow field downstream of the intersection of the two shock waves could be continually monitored for coalescence of the isentropic compression waves. When significant coalescence occurred, the design of the upstream wall generating these waves was modified to reduce the rate of compression, and thus the compression waves were spread further apart. The purpose of spreading the compression waves was to reduce the static pressure gradient at the wall, and to increase the chances of maintaining a full compression turn at the "shoulders" of the cowl and spike compression surfaces, avoiding local expansions for reasons previously mentioned.

The aerodynamic lines of the axisymmetric model thus designed are indicated in Figure 17 along with the faired pressure distributions used to estimate the design point pressure drag. In Figure 18 are the associated laminar skin friction distributions for the cowl and spike. These local values of skin friction coefficient were integrated to estimate the inlet skin friction drag. Results of these internal drag estimates are presented in Figure 19 along with the wetted area distribution for this model. For the total internal drag coefficient of 0.147 the corresponding "drag-equivalent" pressure recovery is 2 percent, whereas the results of the characteristic solution indicated a "core" flow pressure recovery of about η_R = 25 percent. The "core" flow was not the uniform flow as in the simple analytical models used earlier in this report. This additional non-uniformity was caused by the curvature of the initial shock waves. For the design conditions, the calculated "core" flow occupied approximately one third of the constant area duct passage height.

The streamline tracing necessary for determining the internal contours of the swept-lip cowl (Figure 9) posed a particular problem. It was the original intention to use the method of Reference 15. Use of this method requires knowledge of the value of a stream function parameter at each nodal point in the characteristics mesh, and then lines for constant values of this stream function are "traced" through the mesh. Time would not permit development of the computer logic required to permit automatic tracing of selected streamlines, but the characteristics program was modified to calculate the value of the stream function parameter:

$$K_i = \frac{1}{4\sqrt{5}\left(1+\frac{M_i^2}{5}\right)^3 \sin(\beta_i + \theta_i)} \qquad (12)$$

at each of the interior nodal points in the mesh. Large scale plots, based on calculations for the smallest mesh possible consistent with the geometry of interest and machine storage capacity, were then made using the technique indicated in Figure 20. As a check case, a comparison of this technique with the exact treatment given in Reference 16 for cone flow was made. Conical flow was selected as a basis of comparison since the mesh calculation used employs a linear interpolation between two interior points to determine the pressure recovery at the third calculated point (Reference 11). The assumption of constant entropy gradient between nearby interior points in the hypersonic flow, implied by this procedure, has been shown in Reference 17 to be a source of mass flow error. The irrotational field of the conical flow eliminates the effects of this source of error and permits a better assessment of the adequacy of the method of streamline tracing itself. (Prior to this check,

a comparison was made of flow properties at interior points by comparing independent solutions for a cone obtained from Taylor-Macoll theory, and a regular characteristics mesh; the agreement was excellent.) Typical results from the streamline comparison test are presented in Figure 21. The lack of agreement is expected to get progressively worse for hypersonic rotational flow. As a result, use of the stream function technique was abandoned, and a similar method was employed based on lines of constant total pressure recovery. The swept-lip cowl contours thus determined represent only an approximation to the solution sought, based on the calculated axisymmetric cowl shock shape. This is as should be expected, since a boundary layer correction must be made even to the "exact" streamlines. Such boundary layer corrections must necessarily be made for each streamline used. This was accomplished using the same technique employed on the axisymmetric cowl to determine the "physical" wall coordinates. Since the boundary layer calculation procedure used was based on the method of Reference 10, which is applicable to two-dimensional or axisymmetric flow, no allowance was made for the effects of cross flow pressure gradients in the design of the swept-lip cowl.

The coordinates of the swept-lip cowl inlet are presented in Table 1. A key to the interpretation of these coordinates is presented in Figure 22, from which the lines of the axisymmetric cowl can also be determined. Both inlets use the same centerbody design. The swept-lip inlet configuration has the same features as the model of Figure 10, but different surface coordinates.

AERO-MECHANICAL DESIGN CONSIDERATIONS

Several conflicts arise in the translation of the aerodynamic lines described in the previous section, into actual hardware models from which accurate measurements of internal drag can be made. The first of these conflicts is that of internal drag isolation. In the establishment of the "paper" feasibility of determining hypersonic inlet performance from calculations based on force balance internal drag measurements (Reference 6) the assumption was made that the model internal drag could be adequately isolated. One of the objectives of the ensuing experimental program is to establish the validity of this assumption and thus demonstrate the actual practicality of this technique of inlet performance determination. Although force balance drag measurements for external aerodynamic models are quite common, such models do not generally require the same degree (if any) of actual mechanical drag isolation. Although the complete inlet drag (both internal and external) could be measured, some method of subtracting the external drag would have to be devised if the back-calculated values of inlet performance and thermodynamic flow properties are to have any reasonable resemblance to the actual quantities at the exit station of the diffuser.

For these models, this drag isolation is accomplished by the use of metric and non-metric surfaces. Such surfaces are physically isolated from each other and separate balances are used to measure the forces on the metric cowl and the metric spike surfaces. This arrangement is shown schematically in Figure 23. The isolation technique requires the use of small gaps (the order of 0.02 inches wide) to separate the metric and non-metric surfaces. Calculations indicate that less than 1 percent of the inlet mass flow will bleed through these gaps in the constant area throat section. Because of the relatively low balance cavity volume, transient calculations indicate that significant increases in cavity-pressure

(above tunnel ambient) are possible during the few milliseconds of steady state inlet operation. To limit the resulting "thrust" forces on the gap rim in the constant area duct to less than 5 percent of the measured internal drag, provisions have been made for venting the balance cavity, and beveling the gap rim as indicated in Figure 23.

Model size is the second aero-mechanical contradiction. Aerodynamically, it is desirable to test as large a model as possible. Even in those hypersonic test facilities capable of simulating full-scale Unit Reynold's number, the test section size usually limits such tests to small-scale models. As pointed out in Reference 18, for small-scale models the pressure gradients imposed on the inlet boundary layer are more severe than for the full-scale counterpart, and thus there is a greater tendency for boundary layer separation. Although some method of scaling the performance of small-scale inlets may be devised on the basis of Reynold's Number effect on viscous drag, such a technique at the present time, is invalid for the case of separated flow.

The importance of model size, and Unit Reynold's number, when comparing the performance of two inlet models is illustrated in Figure 24. Although the inviscid solution is approached as model scale is increased, the effects of boundary layer transition would eventually increase the viscous drag of the larger models and cause an effective decrease in the "drag-equivalent" pressure recovery.

From a mechanical point of view, a small model is desired. As pointed out in Reference 19, a true representation of the model airload is recovered by adding a signal proportional to the model acceleration, to the balance force signal. In order to produce an acceleration signal of adequate magnitude, the model mass must be minimized. This can be accomplished not only by employing light weight construction techniques, but also by reducing the size of the model.

The maximum capture diameter of these inlet models is 10 inches, which results in a model approximately 3 feet in length. Because of this relatively large model size, it was decided to first build, instrument, and test the axisymmetric configuration, before undertaking the more complex mechanical problems associated with the swept-lip design.

The third and last problem to be discussed in this section is that of internal drag load variation. As pointed out earlier, the duct internal lines were contoured to assure that positive drag loads always act on the cowl and spike metric surfaces. This is desirable because otherwise large thrust forces can act on the back side of these components, causing the balance to measure a net force consisting of a small difference between two large numbers. In addition, this problem becomes amplified when tests must be conducted over a range of Mach numbers and Unit Reynold's numbers. Estimates of cowl and spike component drag loads over the scheduled Reynold's number variation for the Mach range from 8 to 16 in the CAL 48-inch shock tunnel indicated minimum loads of less than one pound to maximum loads approaching 100 pounds.

REFERENCES

1. E. T. Curran and F. D. Stull, (Unclassified Title) "The Potential Performance of the Supersonic Combustion Ramjet Engine," ASD-TDR-63-336, May 1963. (Confidential Report)*

2. C. E. Kepler, J. W. Cnossen and P. E. Demarest, (Unclassified Title) "Hypersonic Inlet Investigations Including Tests to Mach 8.7 and Theoretical Analyses to Mach 15," ASD-TR-61-137, June 1961. (Confidential Report)*

3. D. L. Harshman, J. Keith, J. Weil, et al, (Unclassified Title) "Analytical and Experimental Evaluation of Inlet Compression Systems in the Mach Range 10 to 25", ASD-TDR-63-629, September 1963. (Confidential Report)*

4. P. H. Kutschenreuter, Jr., "Simplified Scram Cycle Analysis for Inlet Performance Investigations," ASRMDF TM 63-9, February 1963.

5. P. H. Kutschenreuter, Jr., "Force Balance Determination of Supersonic/Hypersonic Combustion Inlet Performance Levels," Journal of the Aerospace Sciences," Vol. 29, November 1962.

6. P. H. Kutschenreuter, Jr., "Force Balance Determination of Inlet Performance for Advanced Vehicle Applications to Orbital Velocities Using Internal Drag Measurements," ASD-TDR-63-701, September 1963.

7. R. L. Zurschmeide, "Preliminary Design Considerations for Supersonic/Hypersonic Combustion Force Balance Inlet Model," ASRMM TM 63-4.

8. R. J. Halckinen, I. Greber, et al, "The Interaction of an Oblique Shock Wave with a Laminar Boundary Layer," NASA Memo 2-18-59, March 1959.

9. G. K. Richey, "Applications of Compressible Laminar and Turbulent Boundary Layer Analyses to the Design of Inlet Compression Surfaces," ASRMM TM-63-2, June 1963.

10. C. B. Cohen and E. Reshotko, "The Compressible Laminar Boundary Layer with Heat Transfer and Arbitrary Pressure Gradient," NACA Report 1294, 1956.

11. R. L. Balent, "Application of the Method of Characteristics to Various Inlet Compression Surfaces," ASRMM TM 63-1, June 1963.

12. R. K. Muench, Shock Tunnel Schlieren Photographs Supplied by Cornell Aeronautical Laboratory, May 1963.

13. The Marquardt Corporation (Unclassified Title) "Annual Report, Aerospace Propulsion Program," Vol. VI, Report 5883, March 1962. (Confidential Report)*

---

*No classified material extracted from this report.

14. J. S. Keith, "Boundary Layer Growth and Static Pressure on a Blunted Wedge in Hypersonic Flow," General Electric Report DIM No. 502, Oct 1962.

15. J. C. Evard and S. H. Maslen, "Three-Dimensional Supersonic Nozzles and Inlets of Arbitrary Exit Cross Section," NACA TN 2688, April 1952.

16. Boeing Airplane Company Report D-17880 on "Conical Flow Computations."

17. S. A. Powers and J. B. O'Neill, "Determination of Hypersonic Flow Fields by the Method of Characteristics," AIAA Journal, Vol. 1, No. 7, July 1963.

18, The General Applied Science Laboratories (Unclassified Title) Report Nr. 3, "Analytical and Experimental Evaluation of Hypersonic Ramjet," QR-3-5531, November 1962. (Confidential Report)*

19. J. F. Martin, G. R. Duryen, and L. M. Stevenson, "Instrumentation for Force and Pressure Measurements in a Hypersonic Shock Tunnel," CAL Report Nr. 113, January 1962.

*No classified material extracted from this report.

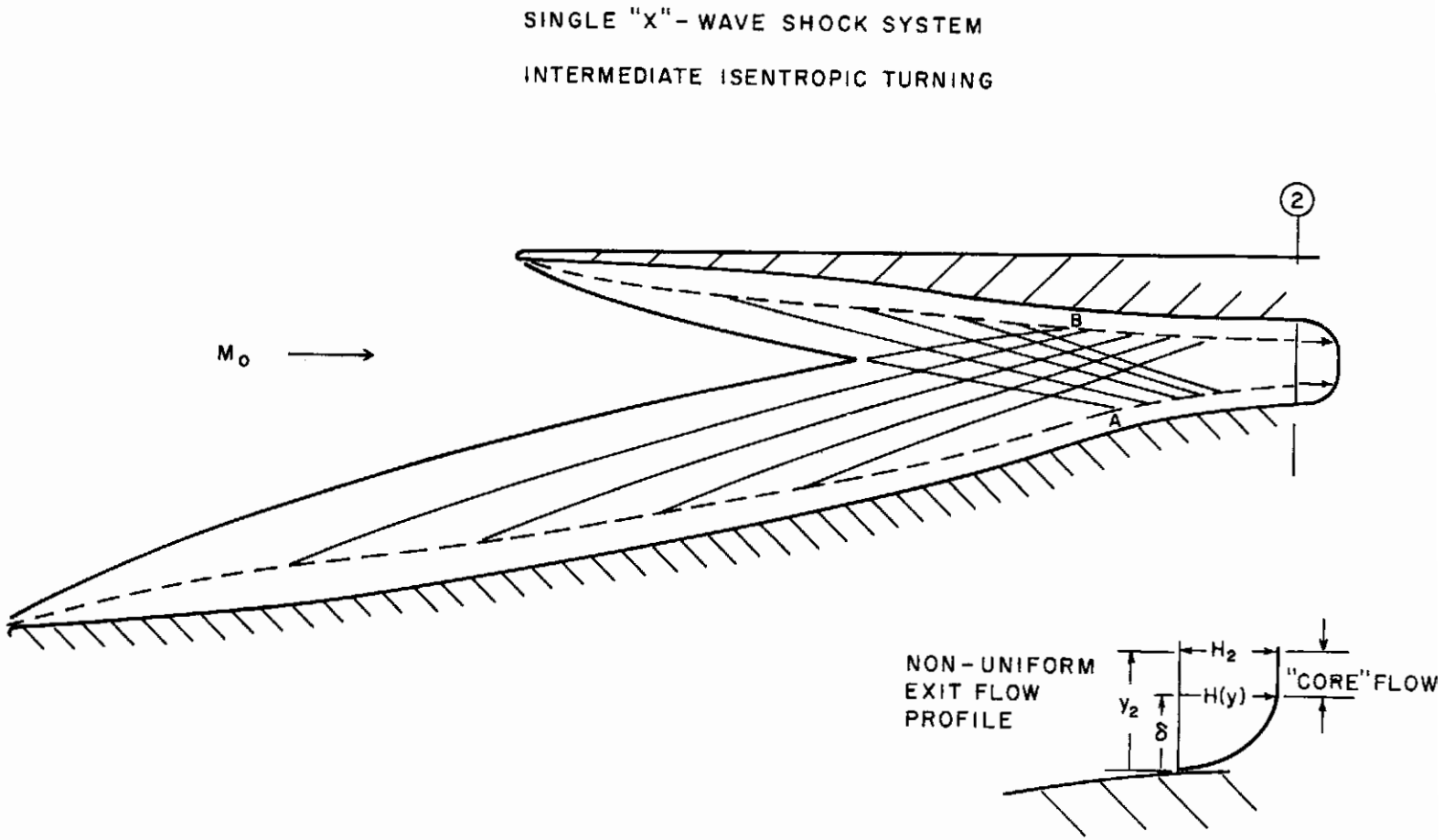

Figure 1. Supersonic Burning Ramjet Inlet Flow System Schematic

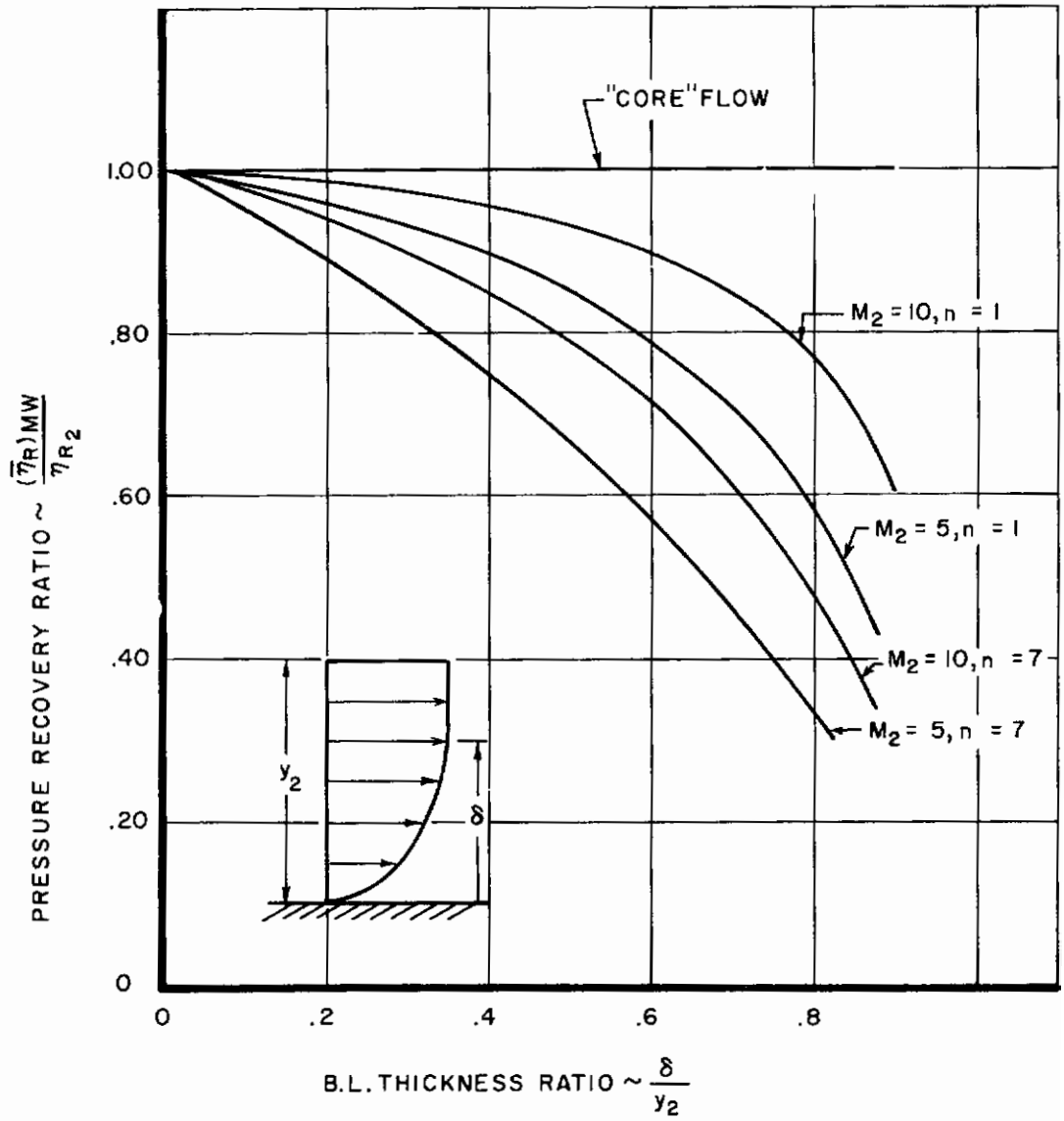

Figure 2. Comparison of "Core" Flow and Mass Weighted η_R

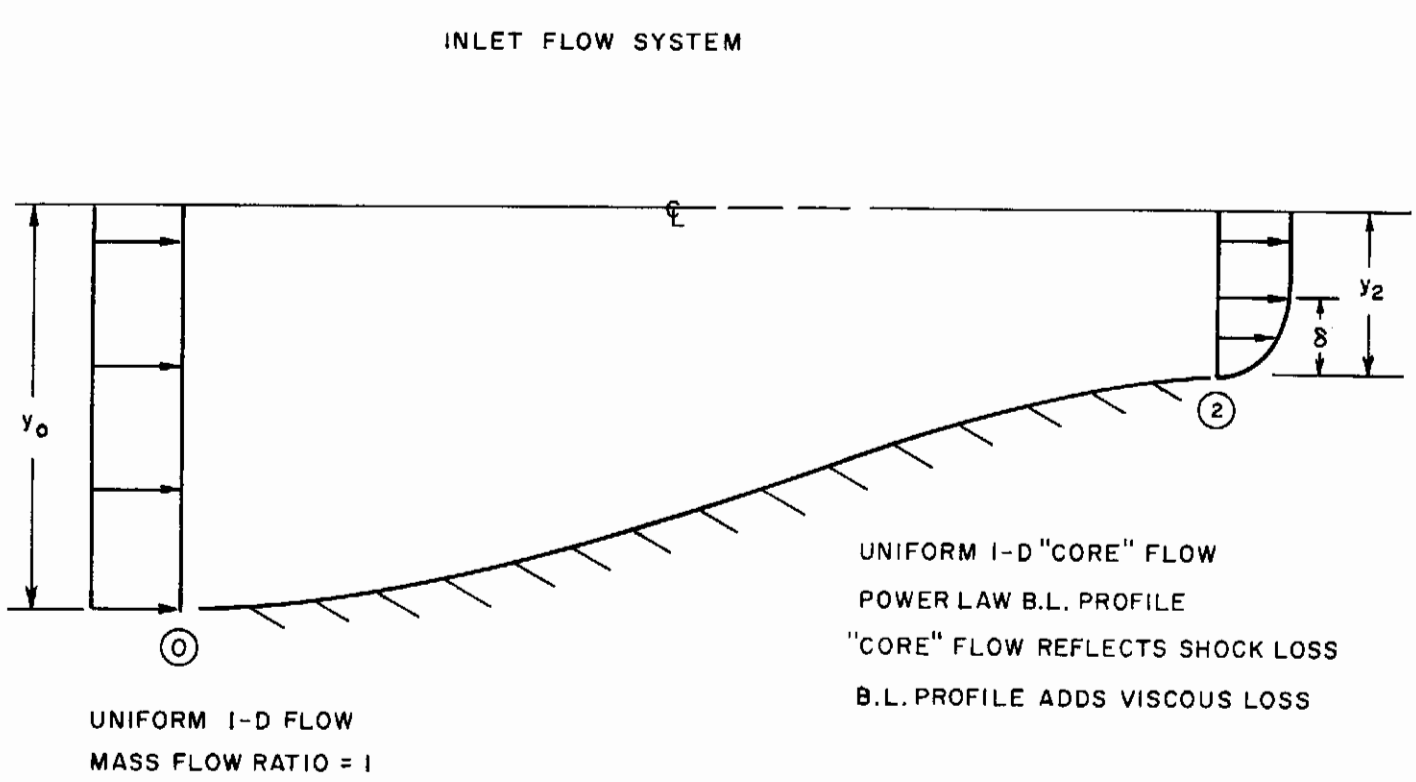

Figure 3. Schematic of Flow System used for Figures 4 and 5

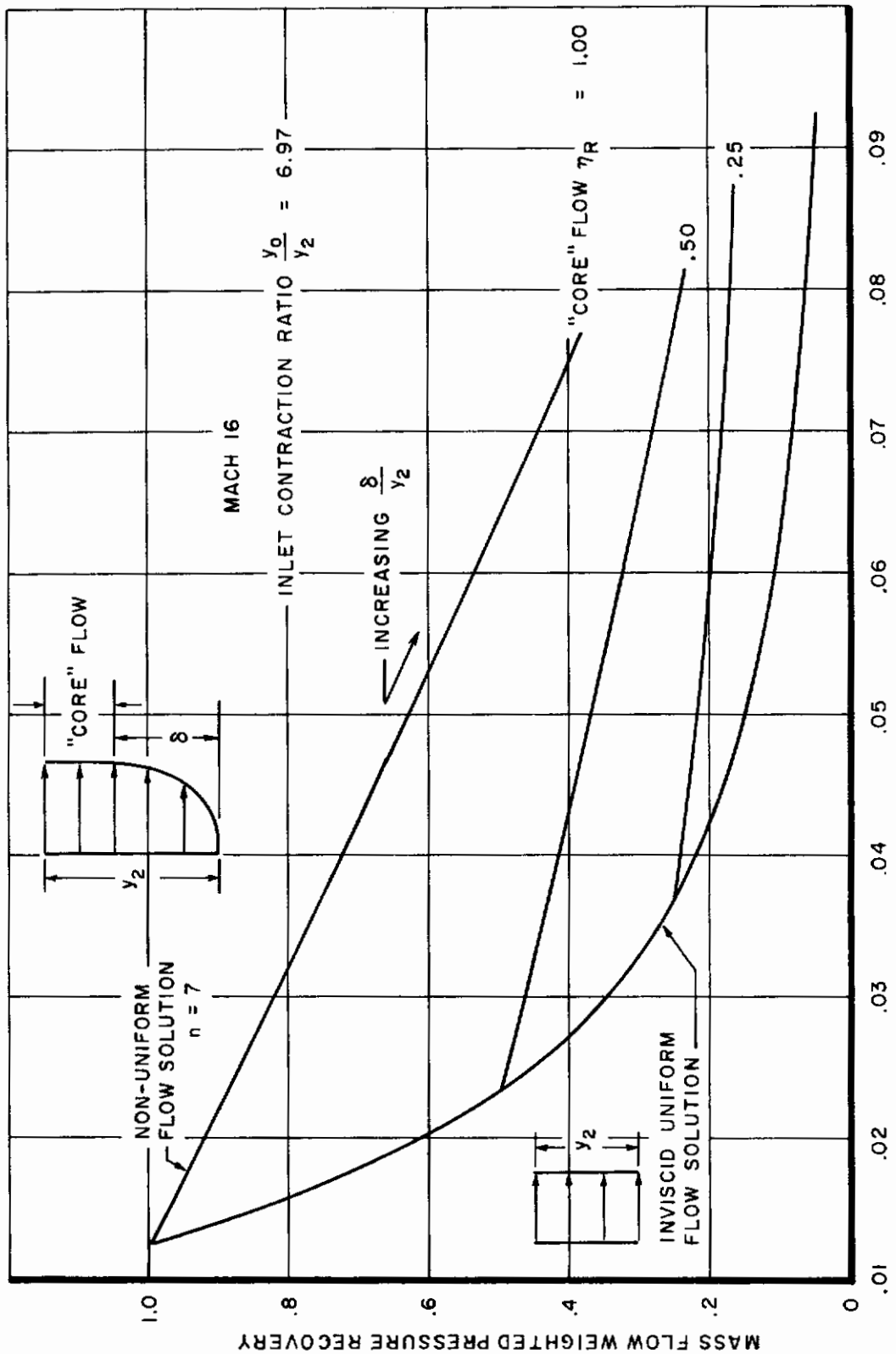

Figure 4. Mass Flow Weighted Pressure Recovery vs Internal Drag Coefficient

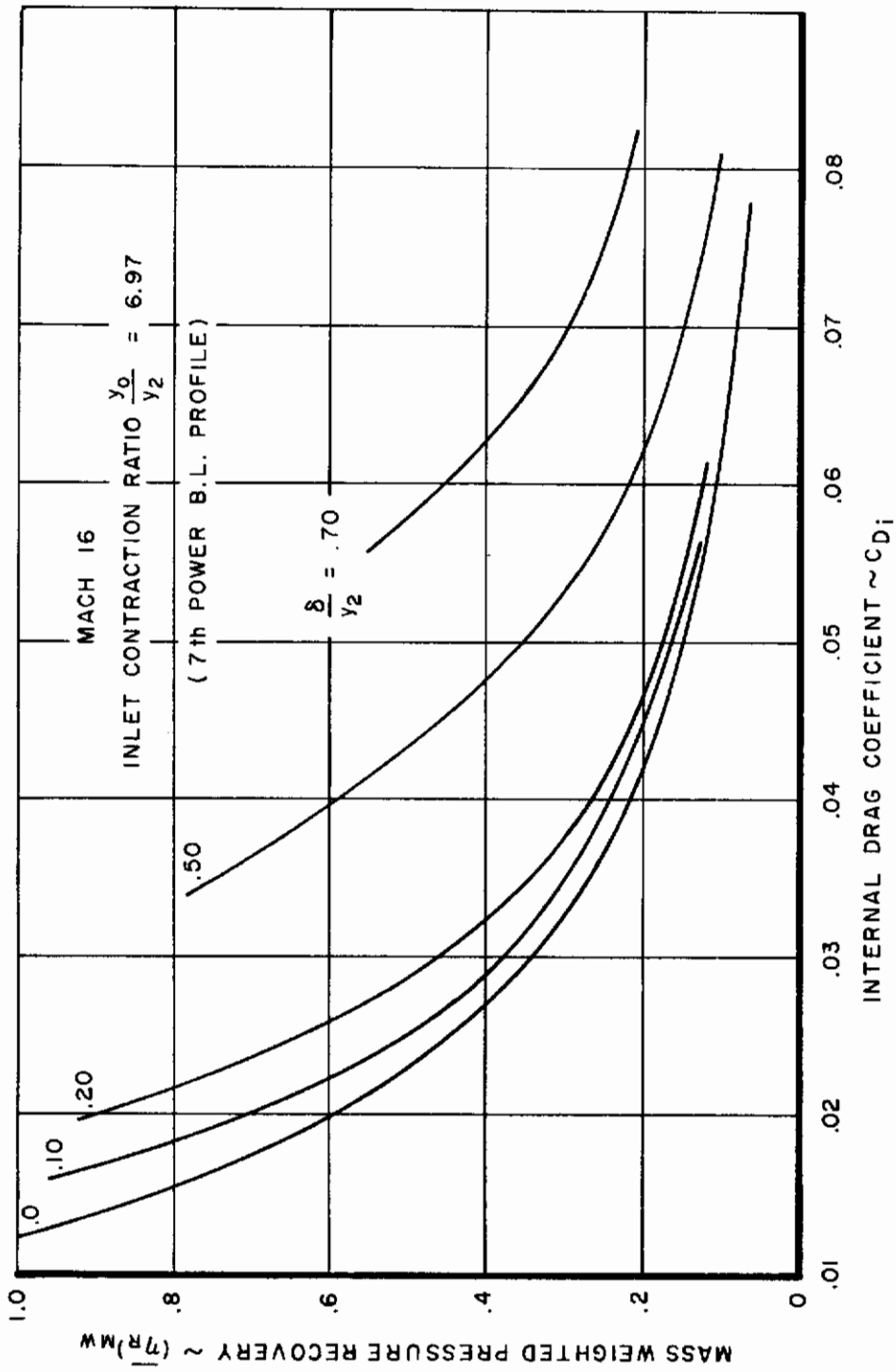

Figure 5. Effect of Boundary Layer Thickness Ratio on η_R and C_{D_i}

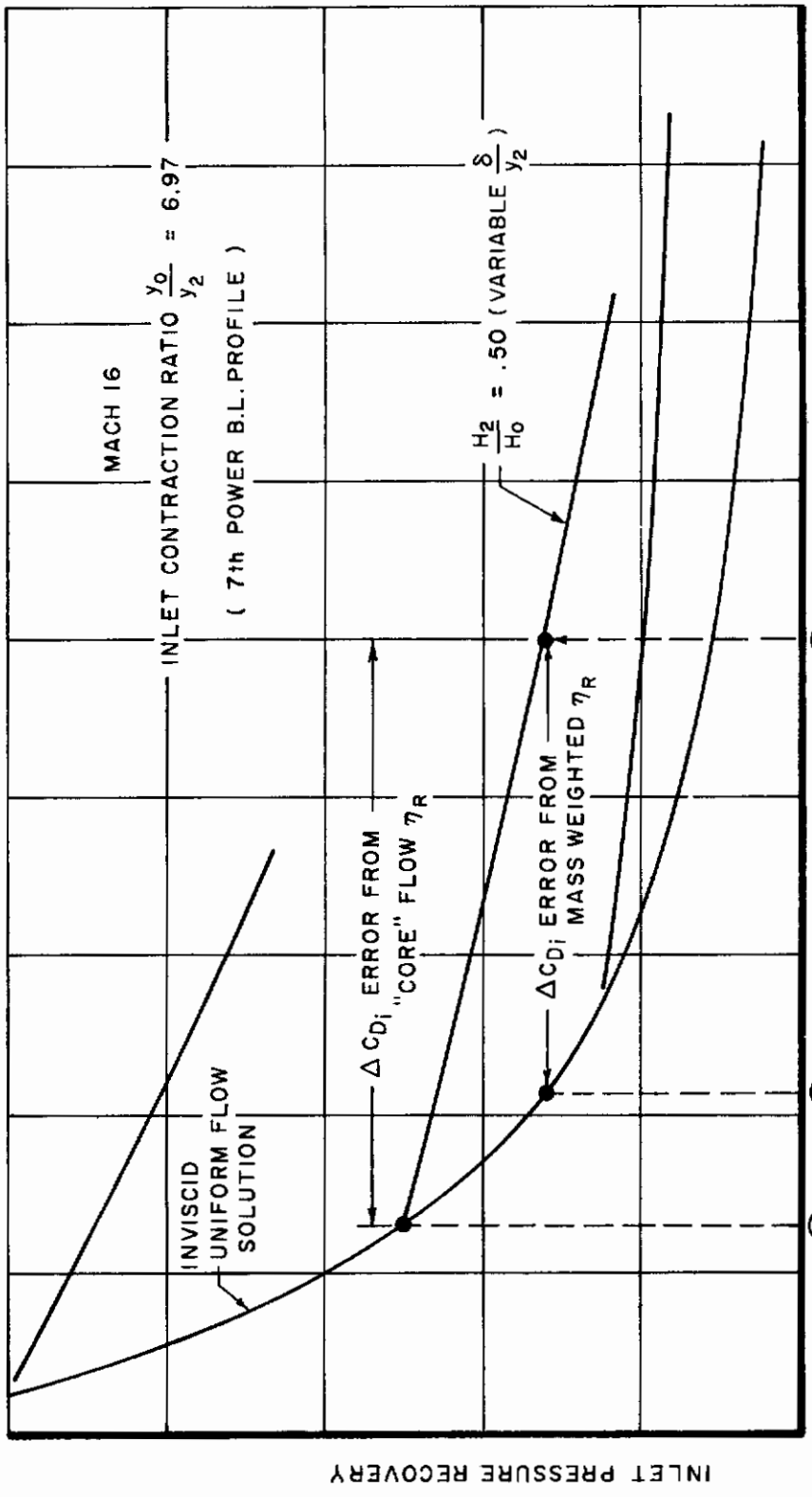

Figure 6. Effect of Pressure Recovery on Inlet Drag Error

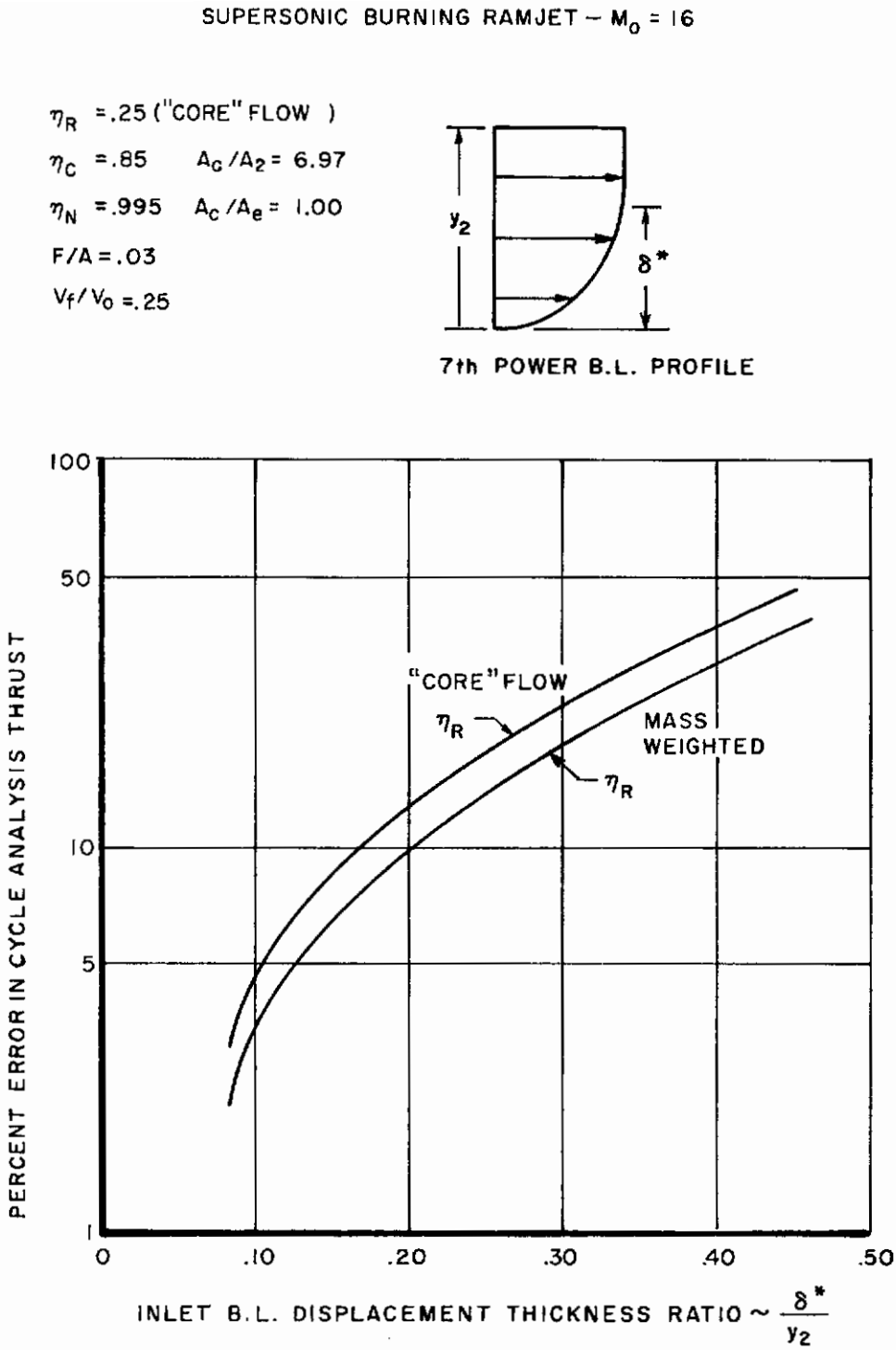

Figure 7. Effect of C_{D_i} Error on Cycle Computed Net Thrust

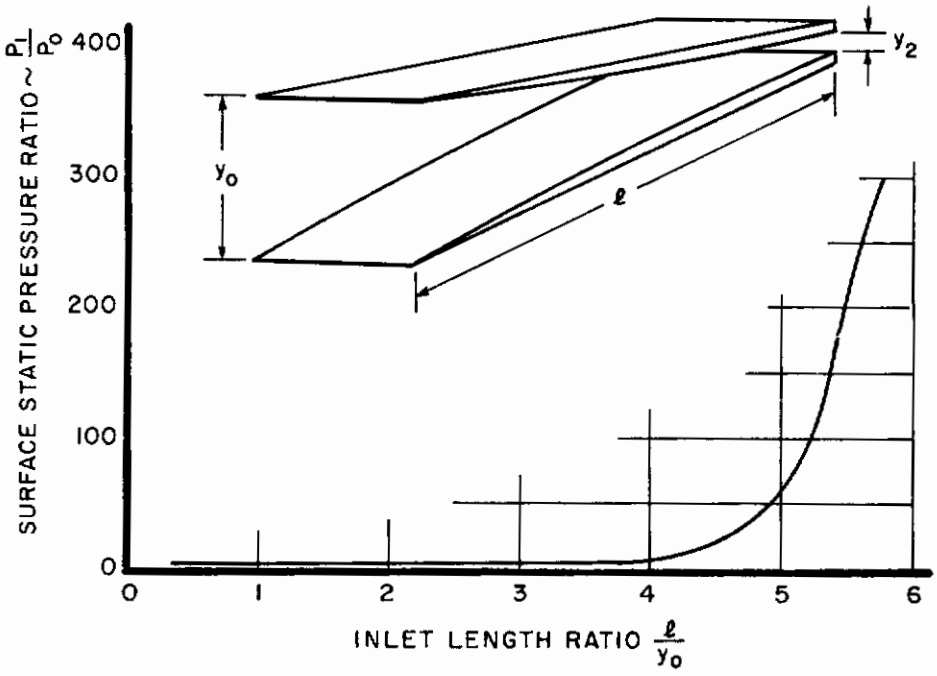

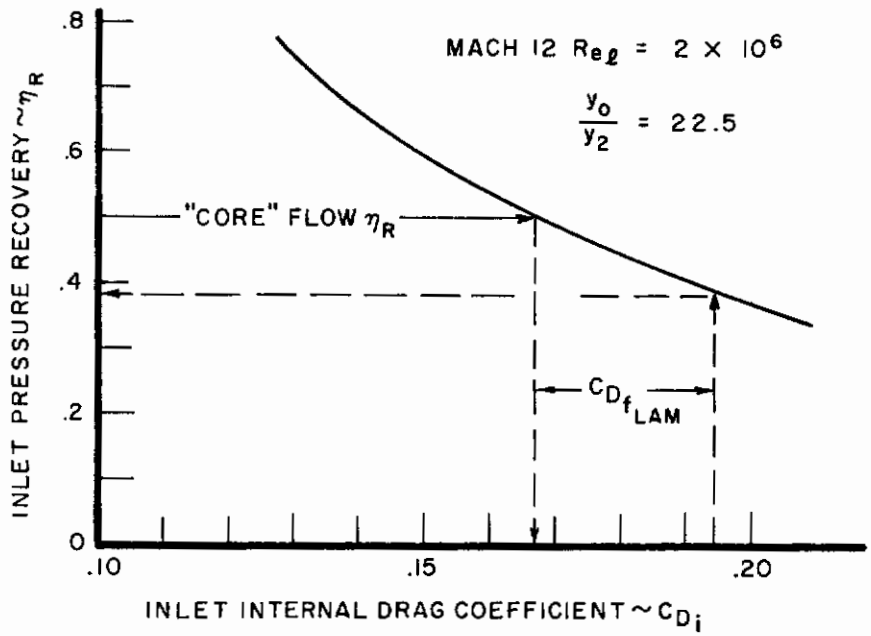

Figure 8. Effect of Inlet Friction Drag on "Core" Flow η_R

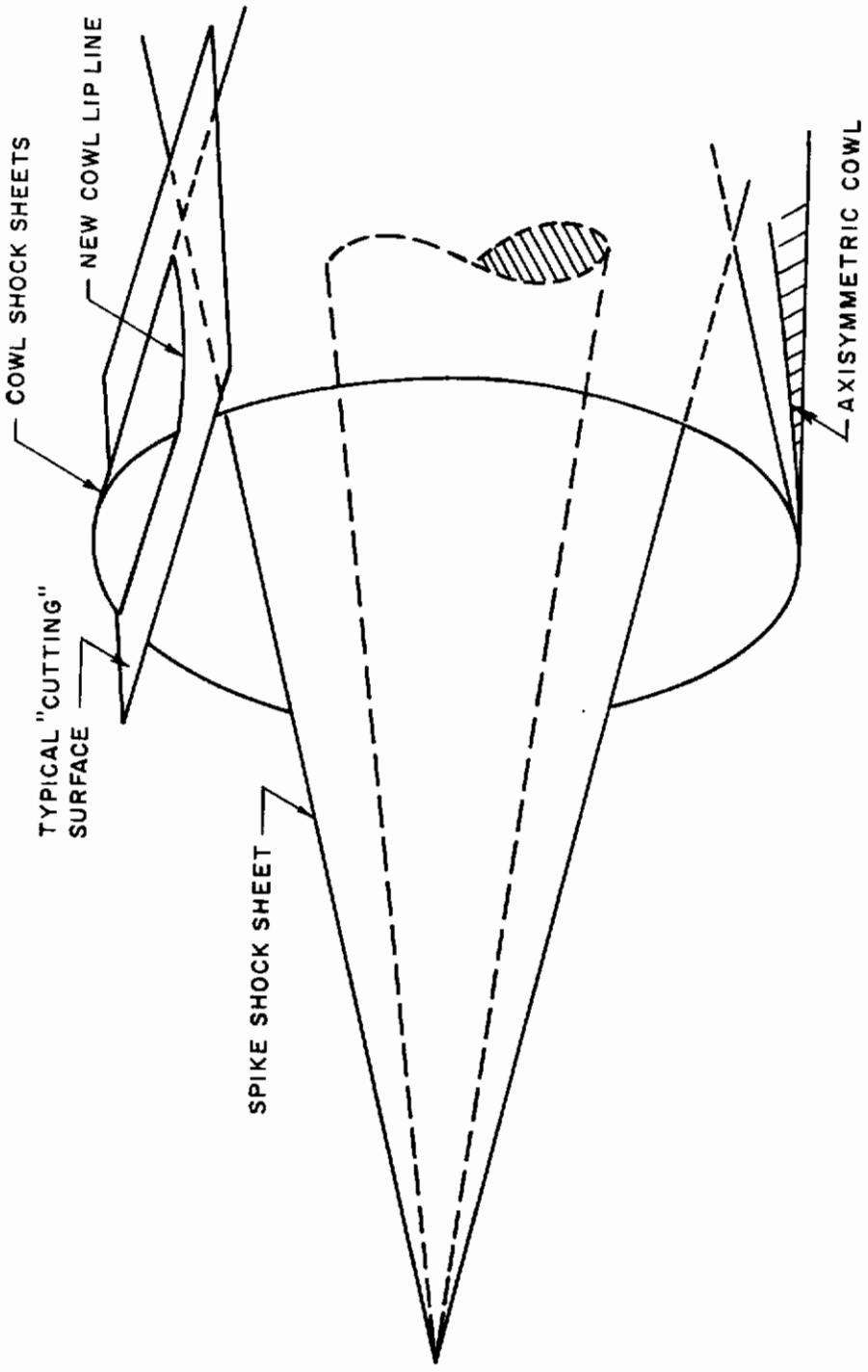

Figure 9. Method for Generating Swept-Lip Cowl Leading Edge Coordinates

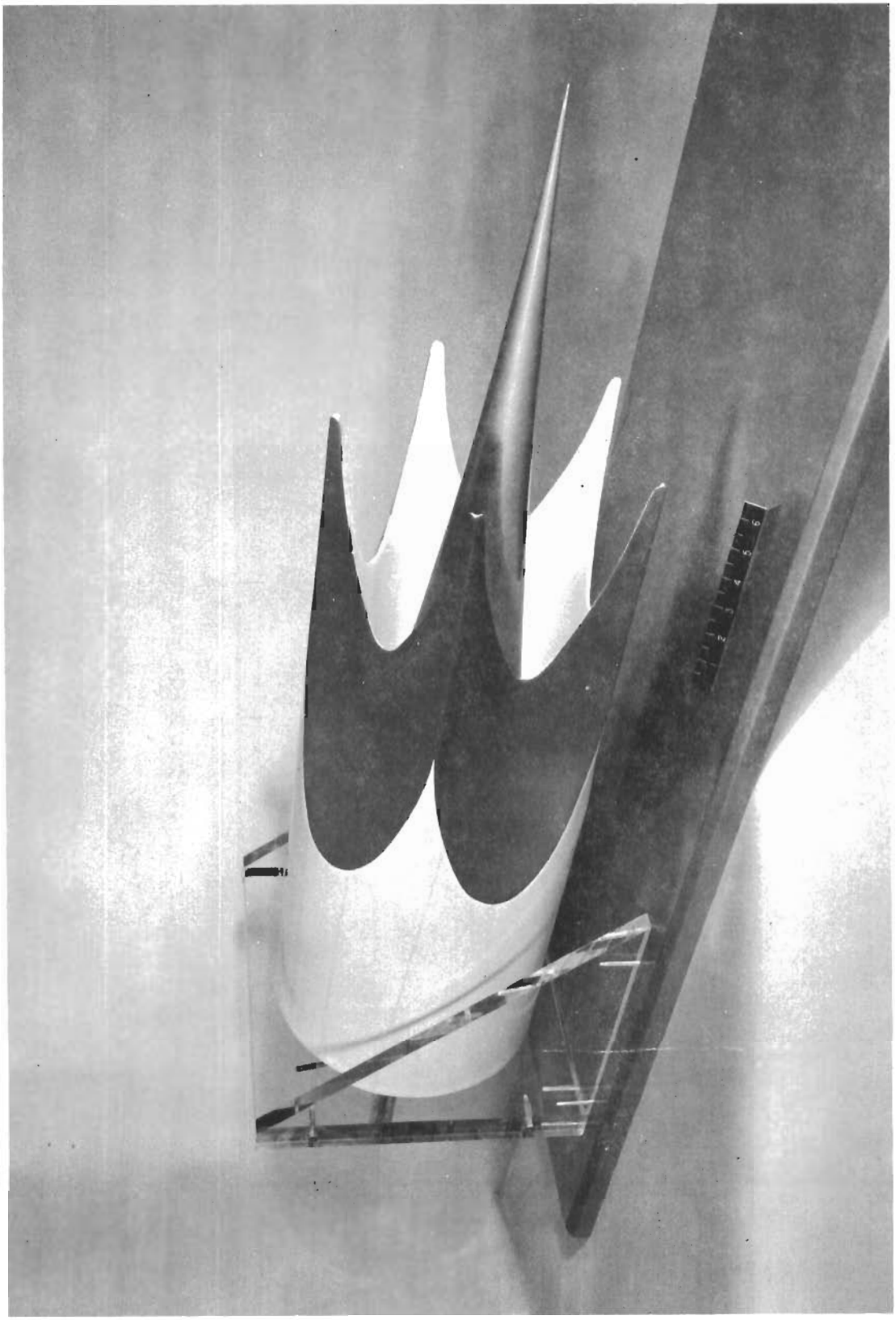

Figure 10. Hypersonic Inlet Model

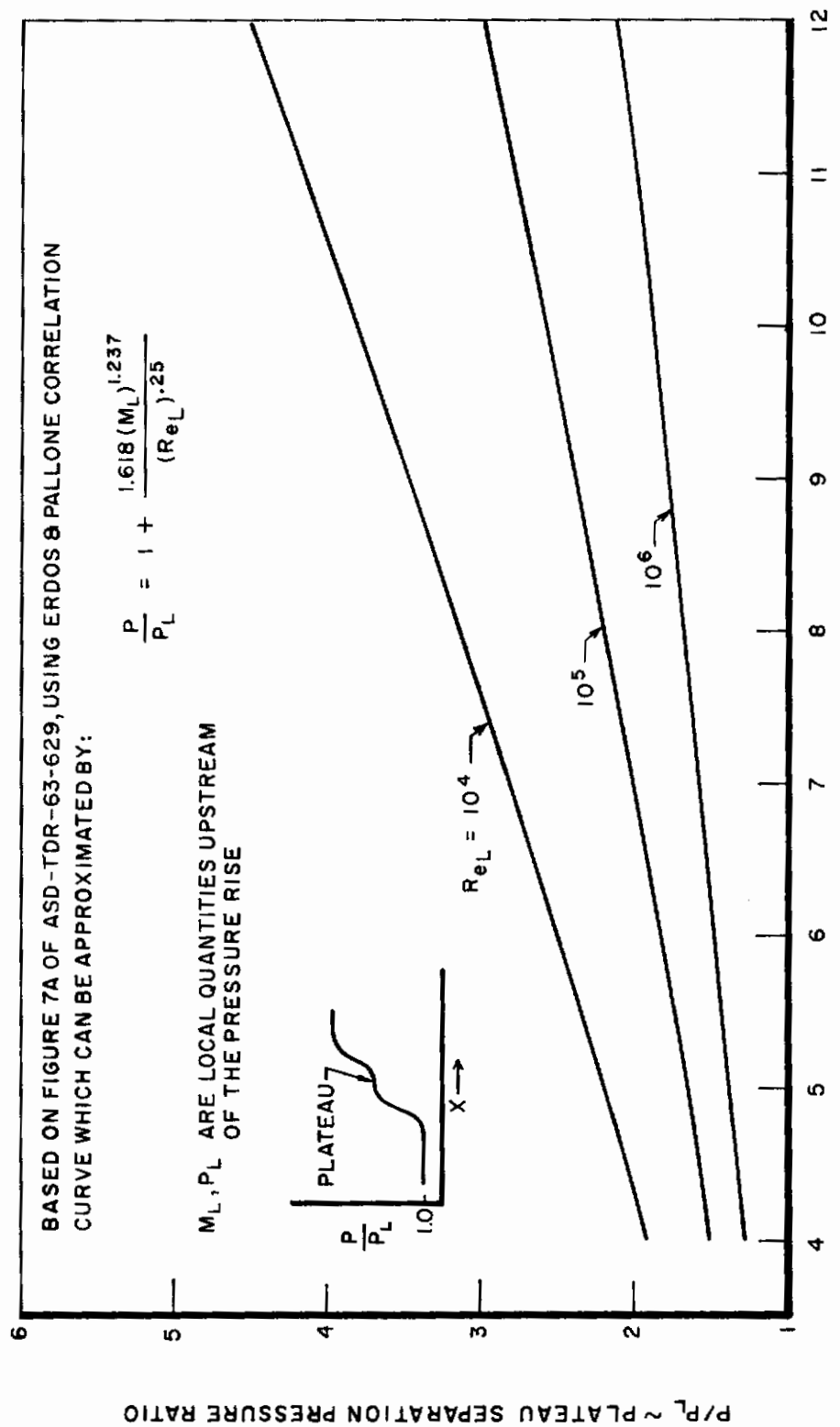

Figure 11. Laminar Boundary Layer Plateau Separation Pressure Ratio

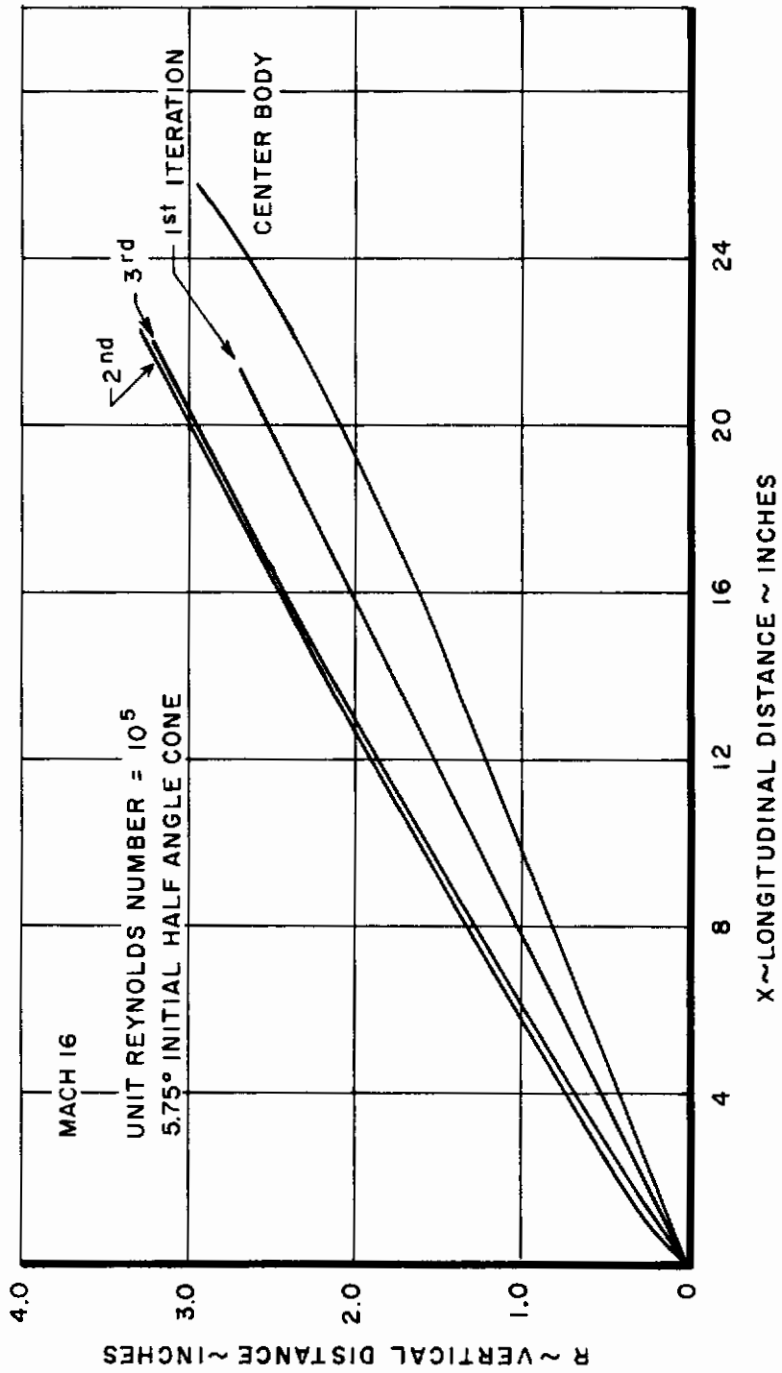

Figure 12. Results of Spike Shock Shape Iterations

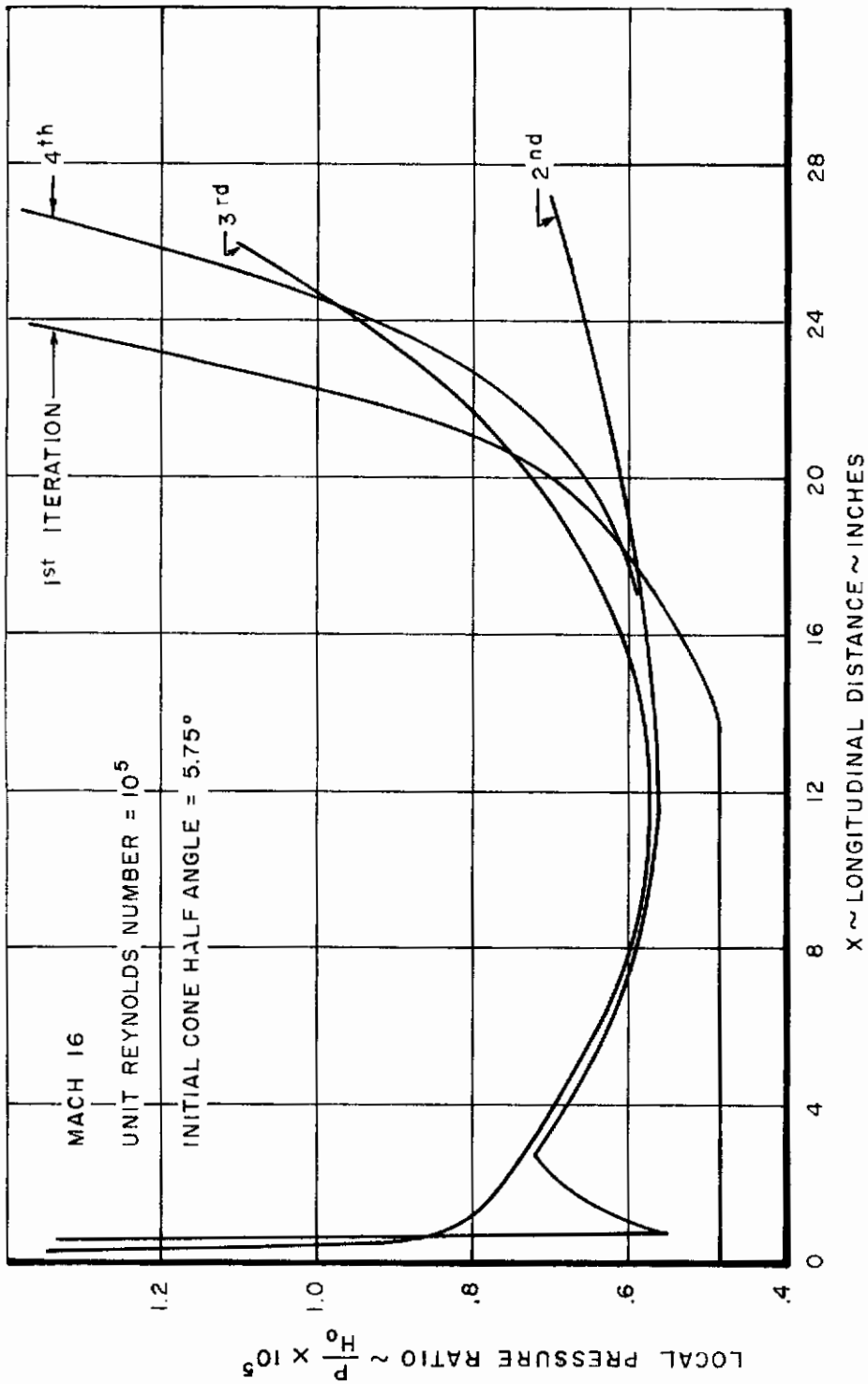

Figure 13. Results of Spike Flow Field Iterations on Surface Pressure

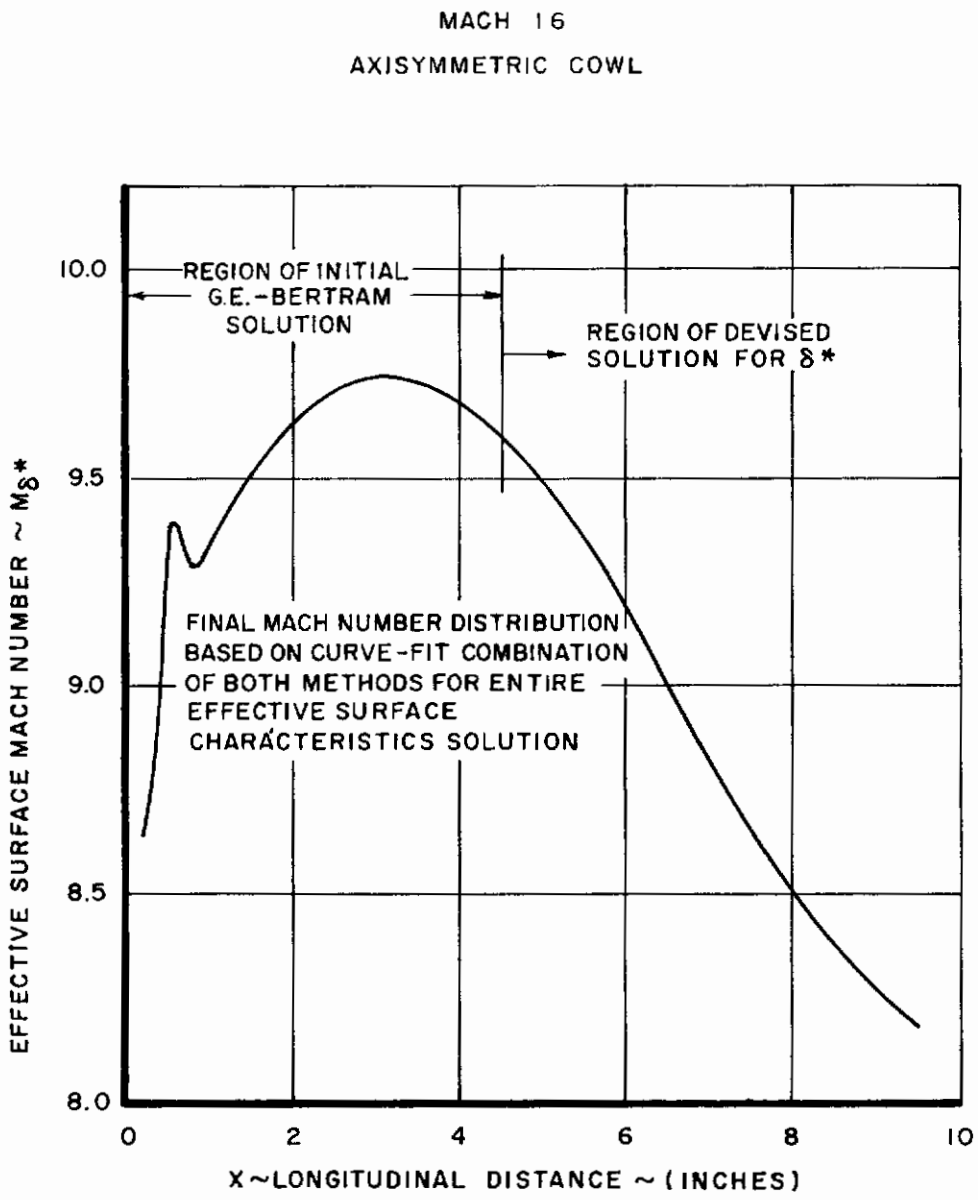

Figure 14. Cowl Effective Surface Mach Number Distribution

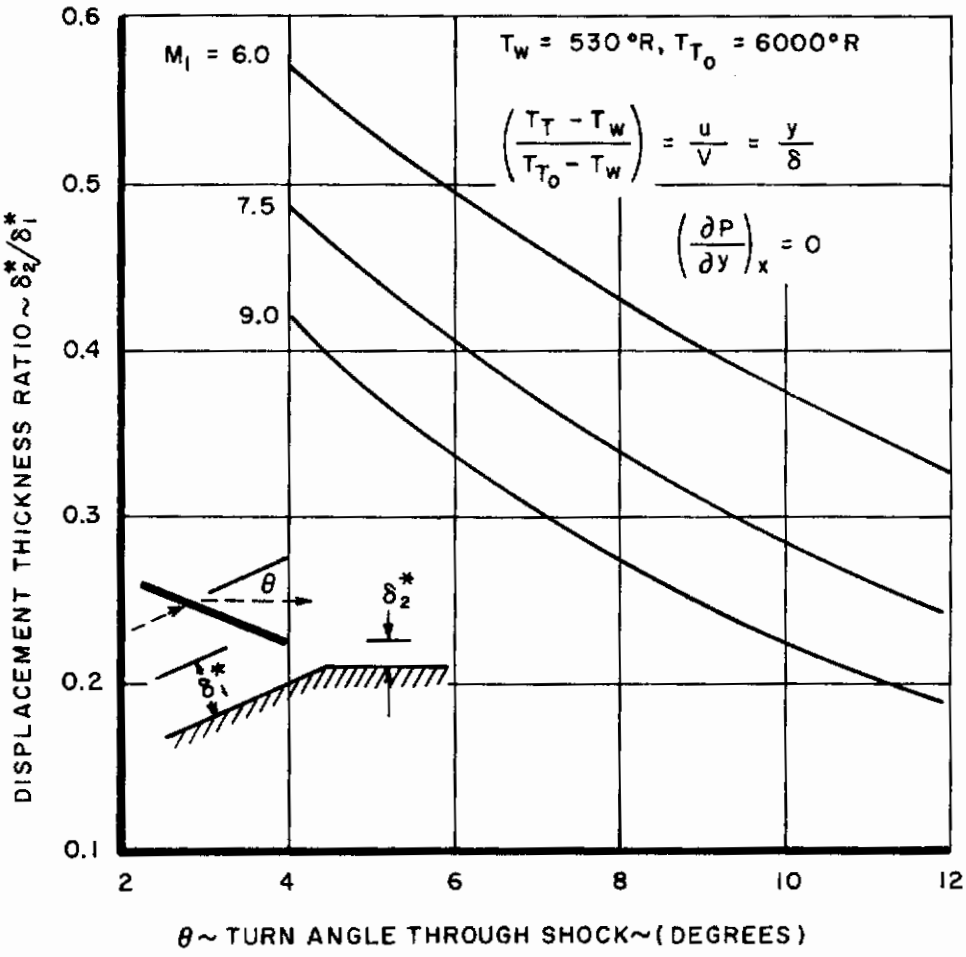

Figure 15. Displacement Thickness Ratio vs Turn Angle

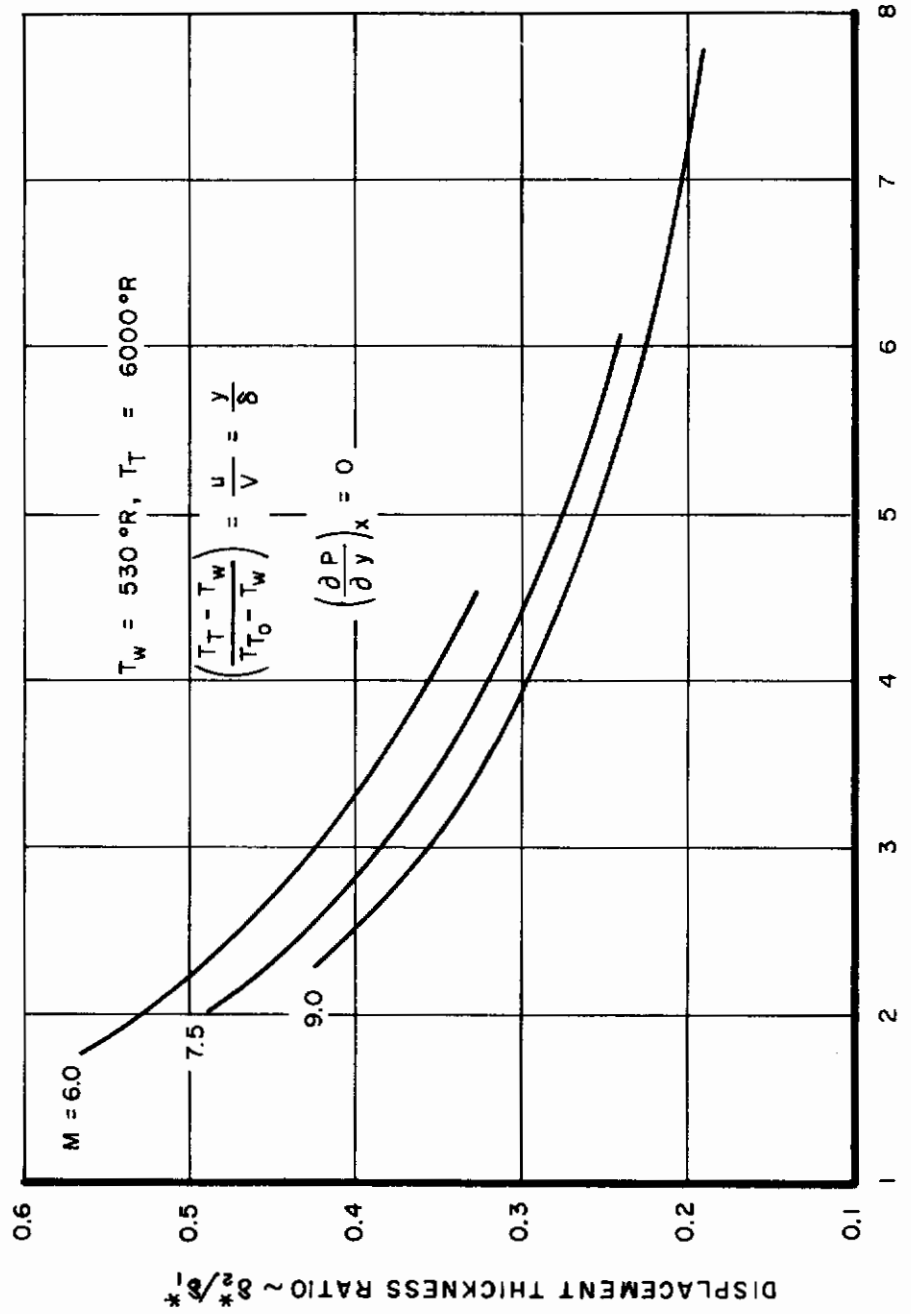

Figure 16. Displacement Thickness Thinning Through a Non-reflected Shock

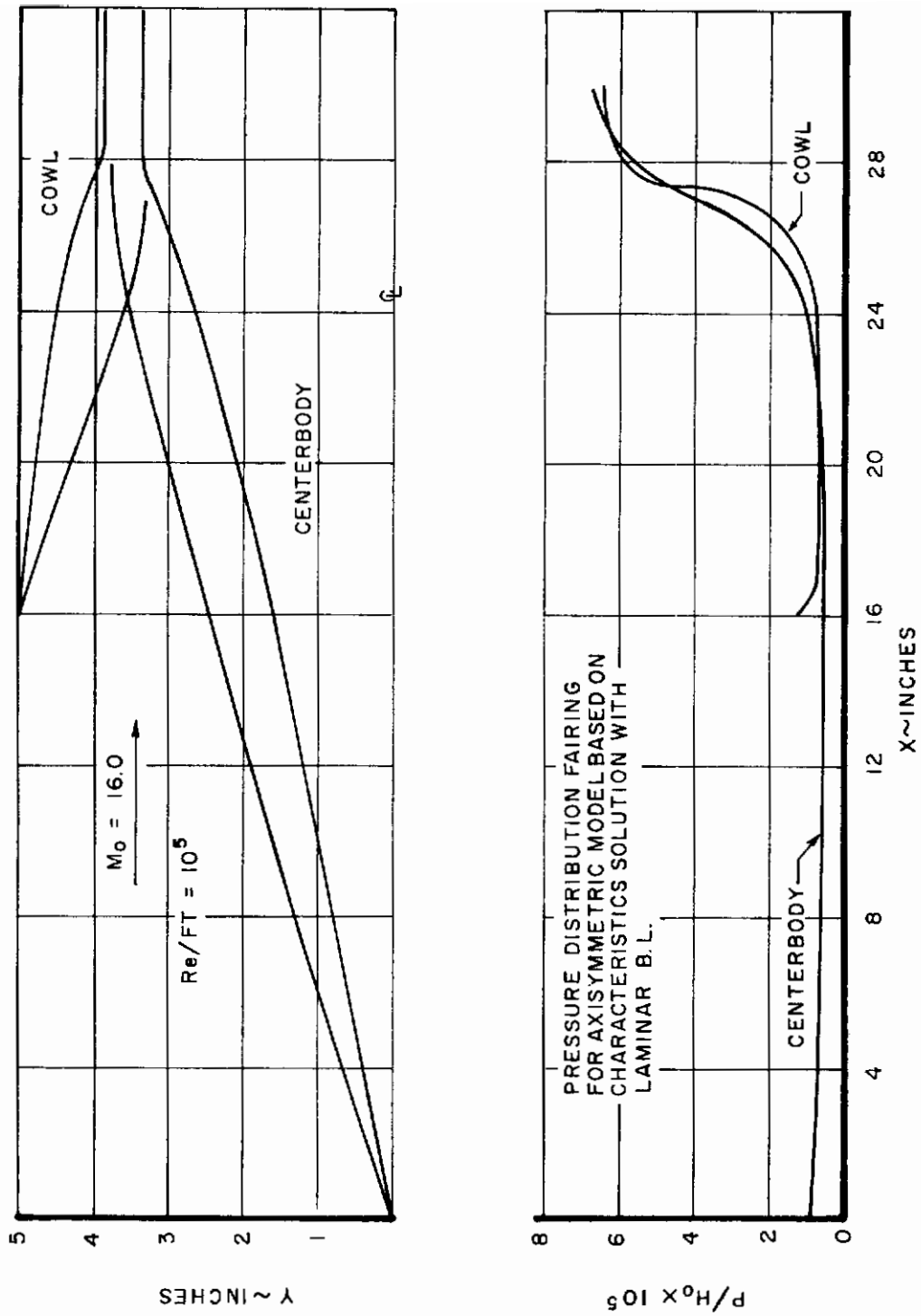

Figure 17. Composite Lines Sketch and Pressure Distribution

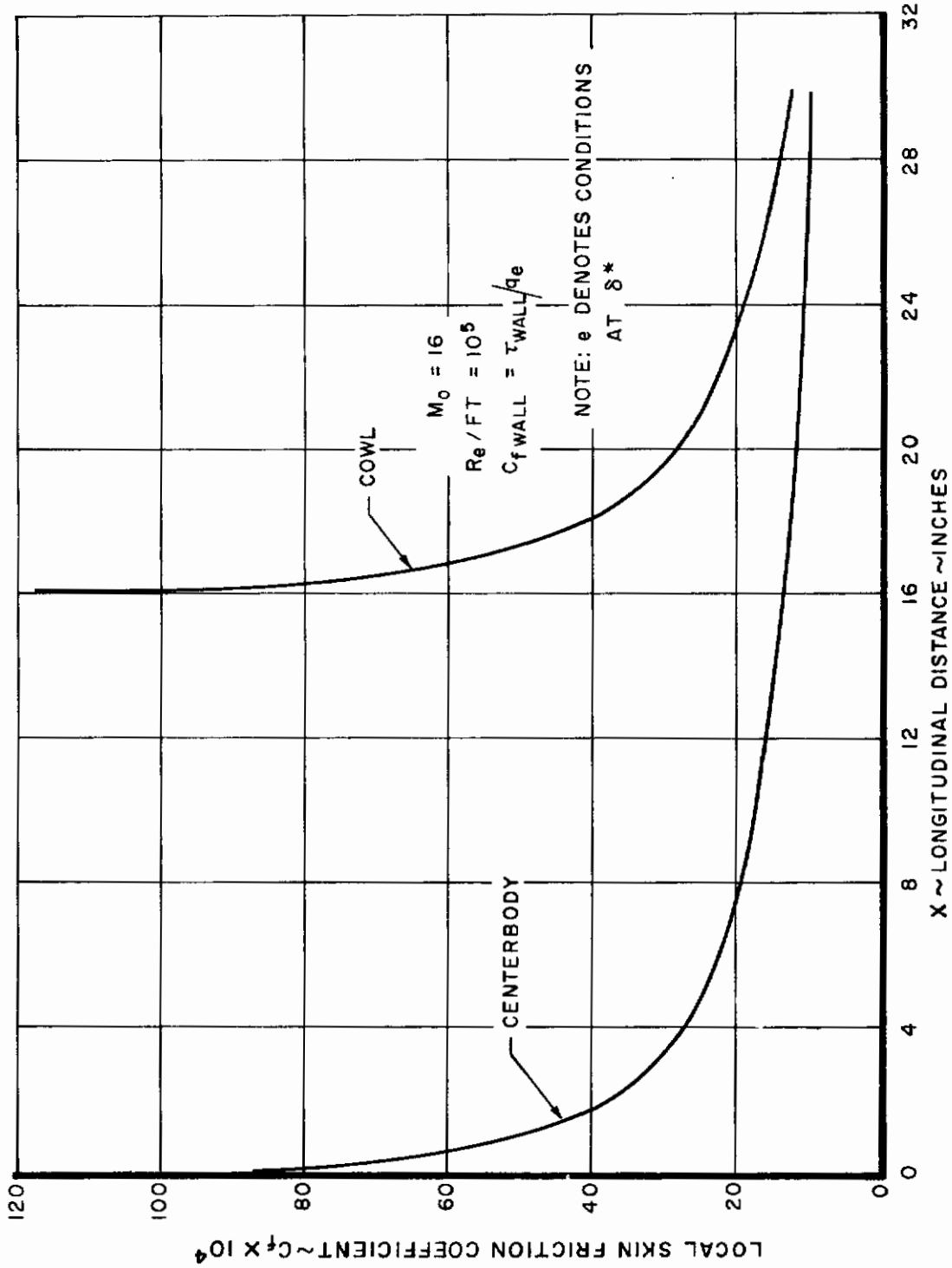

Figure 18. Axisymmetric Inlet Local Skin Friction Distribution

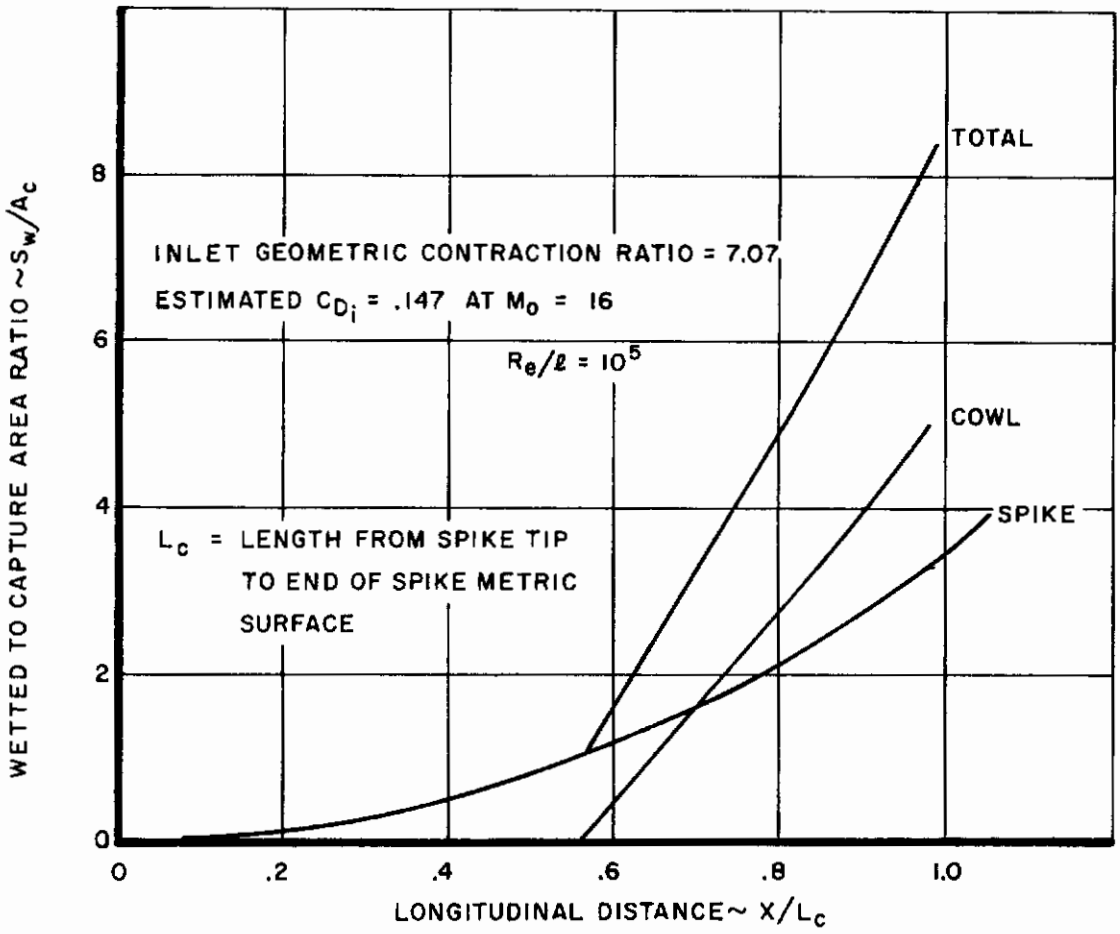

Figure 19. Wetted Area Distribution for Axisymmetric Inlet

AT EACH NODAL POINT:

$$K_i = \frac{1}{4\sqrt{5}\left(1+\frac{M_i^2}{5}\right)^3 \sin(\beta_i+\theta_i)}$$

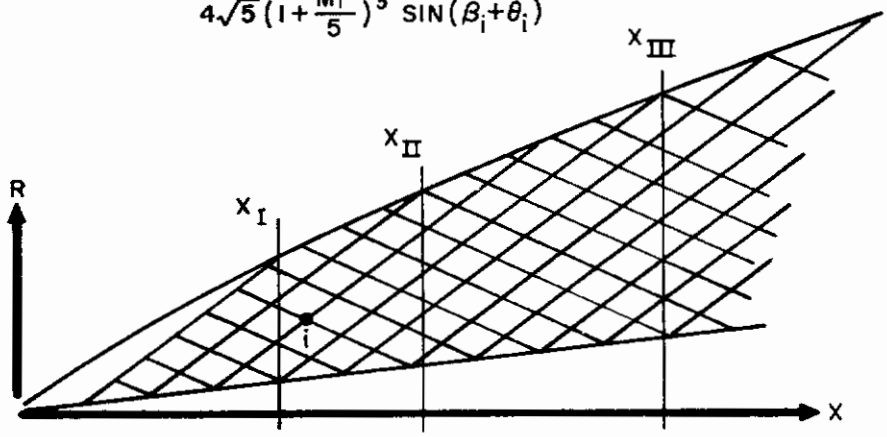

$$\Delta\psi = (K_i + K_{i-1})(R_i^2 - R_{i-1}^2)$$

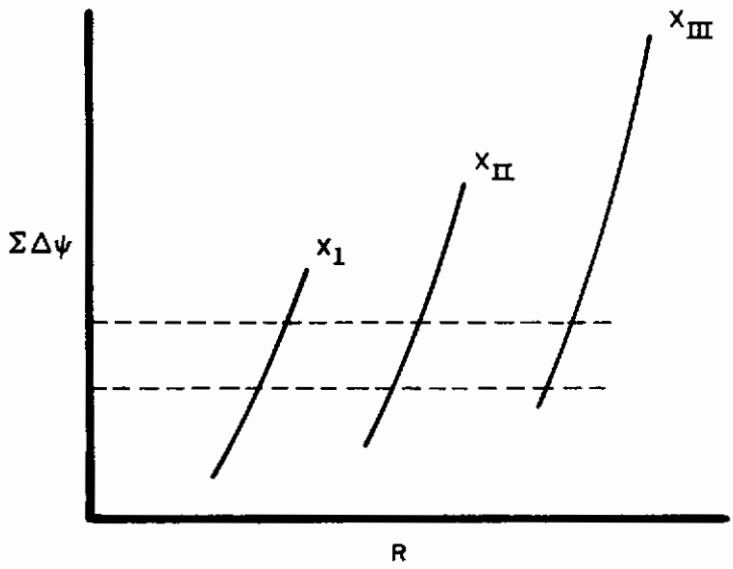

Figure 20. Streamline Tracing Technique

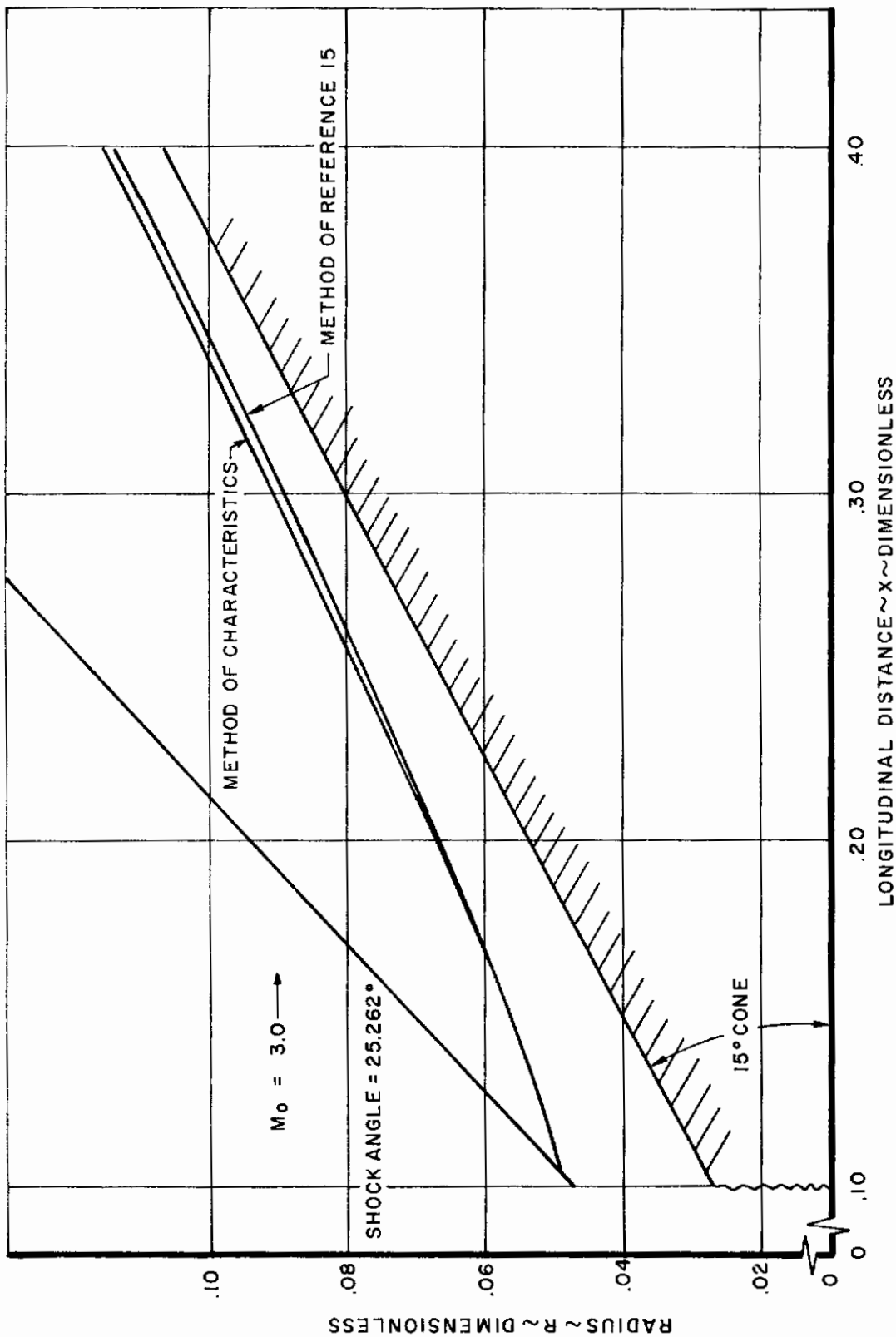

Figure 21. Streamline Comparison

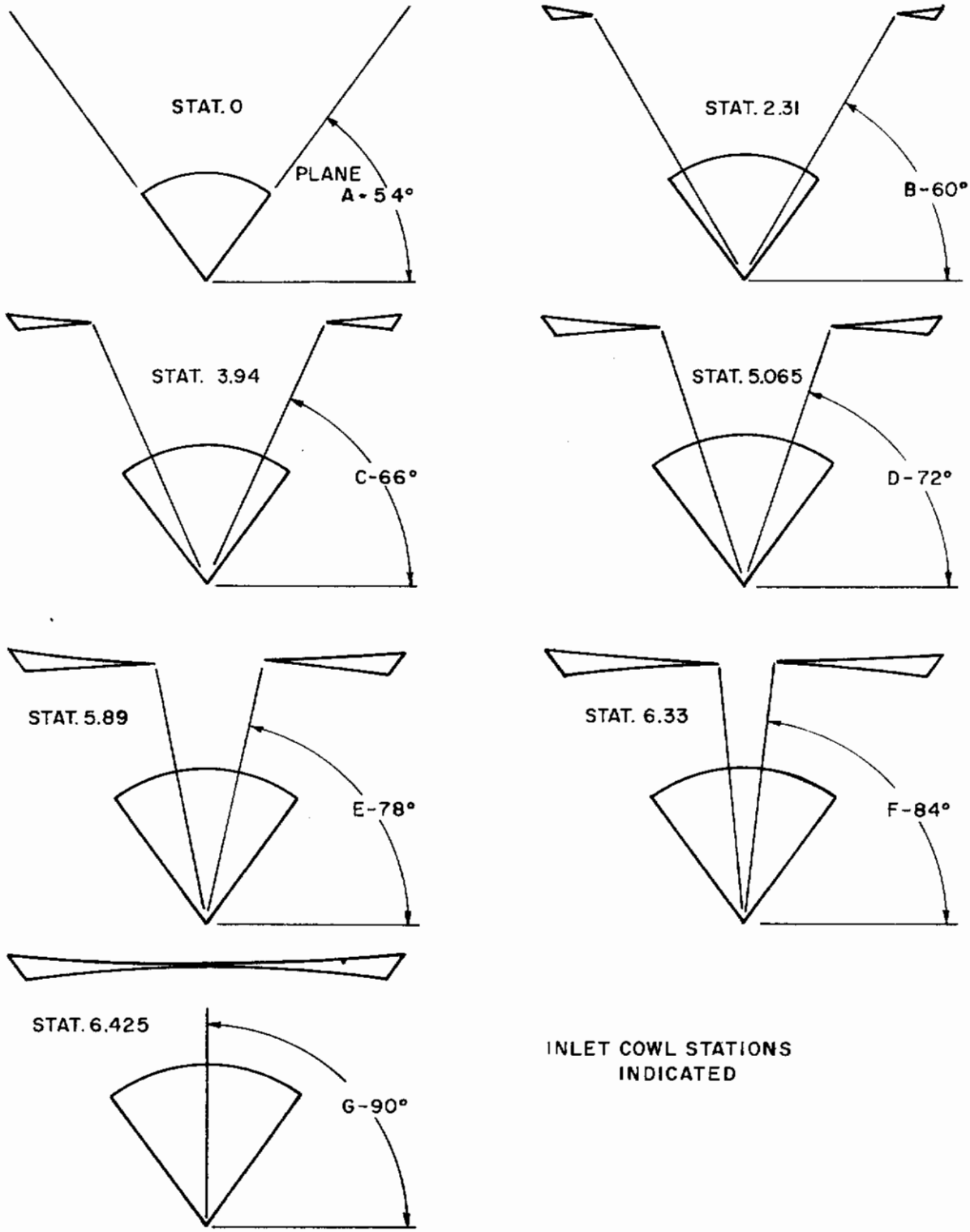

Figure 22. Swept-Lip Inlet "X"-Sections and Key to Table 1

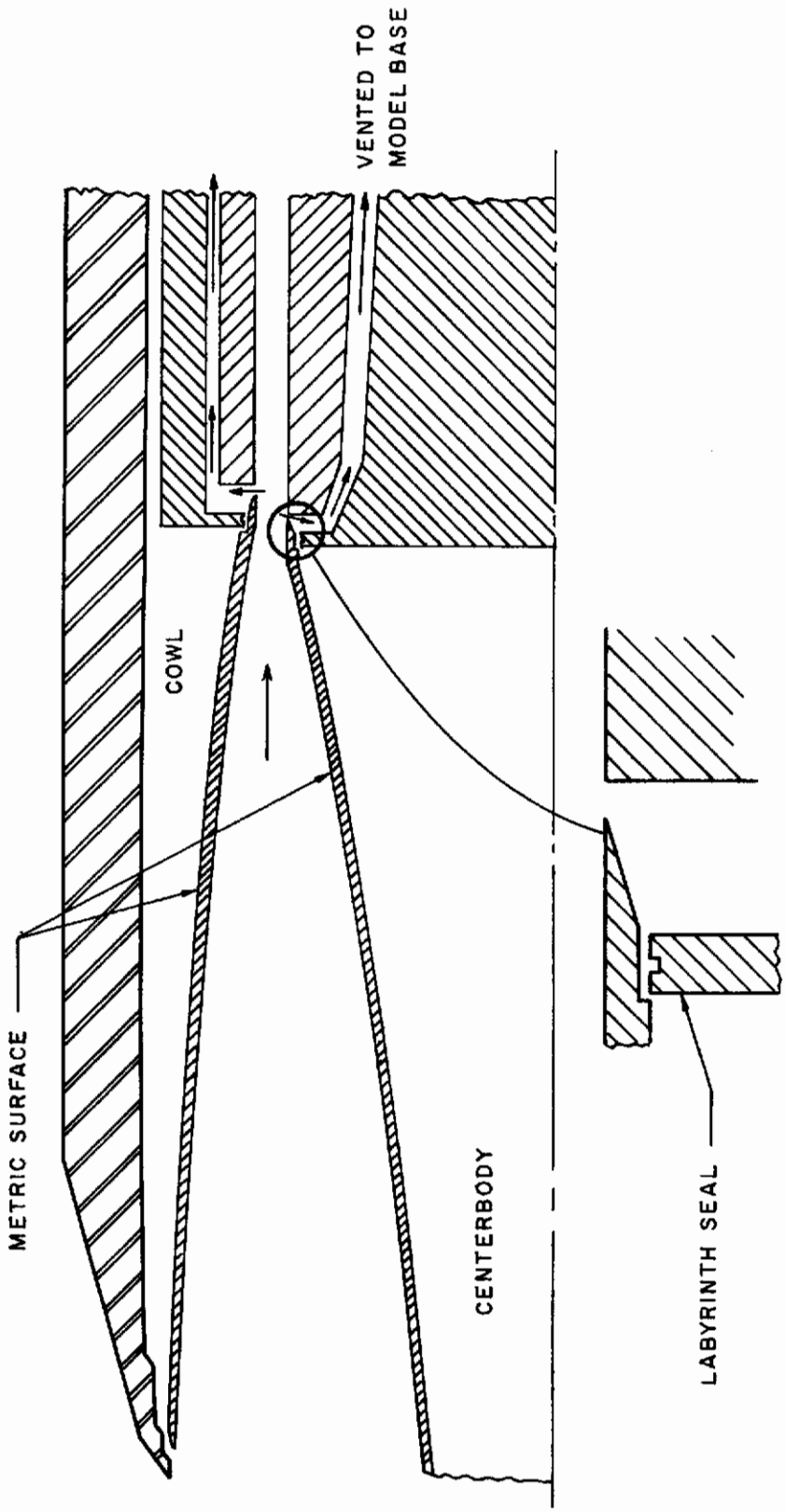

Figure 23. Model Drag Isolation Schematic

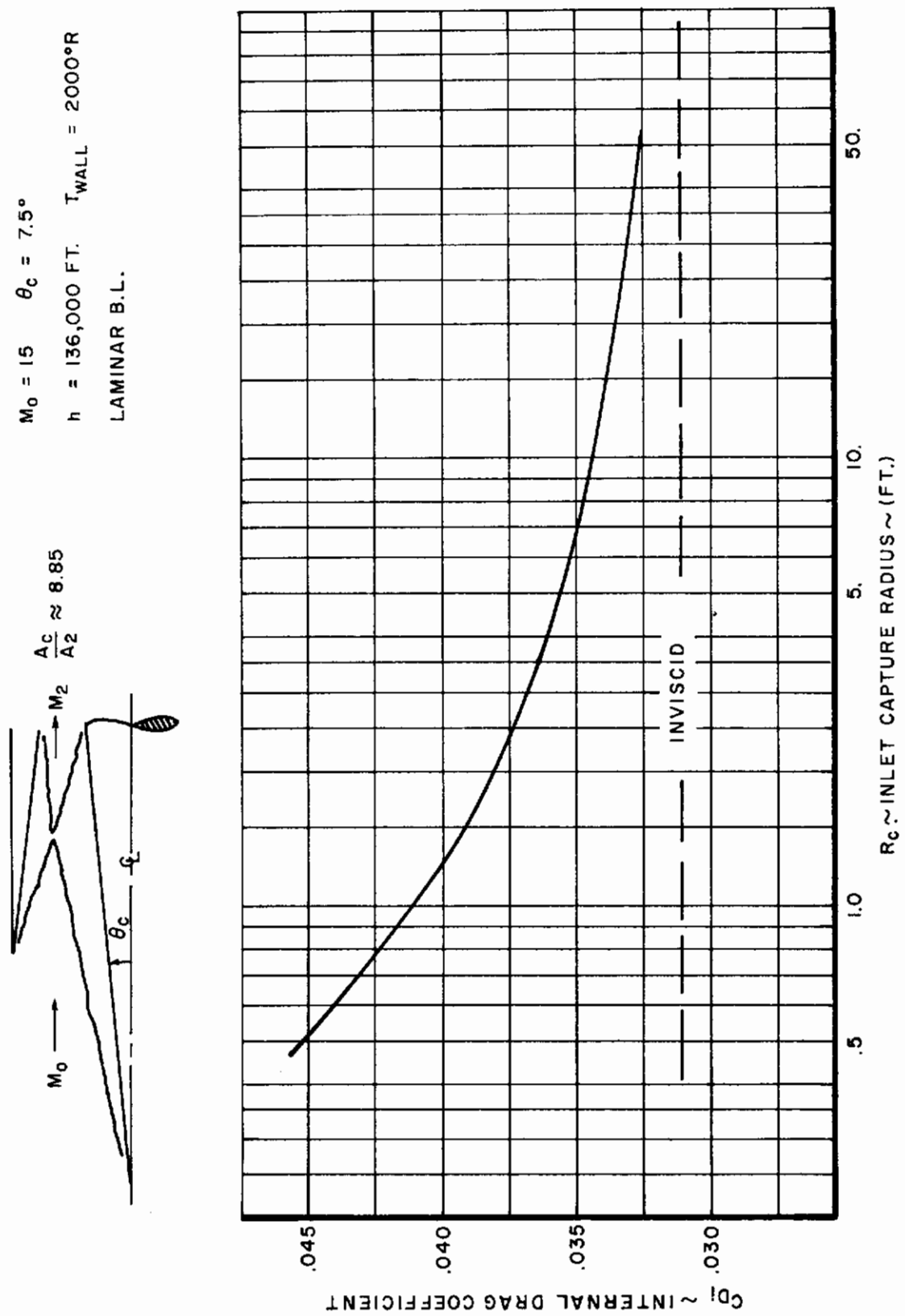

Figure 24. Effect of Model Scale on Internal Drag

TABLE 1
SWEPT-LIP COWL INLET COORDINATES

PLANE A		PLANE B		PLANE C		PLANE D		PLANE E	
X	Y	X	Y	X	Y	X	Y	X	Y
0.000	5.000	2.310	4.554	3.940	4.269	5.065	4.078	5.890	3.939
0.500	4.977	3.000	4.520	4.500	4.245	5.500	4.053	6.500	3.908
1.000	4.952	3.500	4.496	5.000	4.222	6.000	4.026	7.000	3.880
1.500	4.925	4.000	4.471	5.500	4.193	6.500	3.995	7.500	3.844
2.000	4.896	4.500	4.441	6.000	4.153	7.000	3.960	8.000	3.808
2.500	4.868	5.000	4.406	6.500	4.115	7.500	3.922	8.500	3.772
3.000	4.836	5.500	4.370	7.000	4.076	8.000	3.885	9.000	3.730
3.500	4.801	6.000	4.330	7.500	4.038	8.500	3.849	9.500	3.696
4.000	4.768	6.500	4.288	8.000	4.000	9.000	3.808	10.000	3.663
4.500	4.734	7.000	4.245	8.500	3.959	9.500	3.775	10.100	3.658
5.000	4.696	7.500	4.200	9.000	3.917	10.000	3.733	10.200	3.656
5.500	4.660	8.000	4.152	9.500	3.872	10.500	3.699	10.300	3.652
6.000	4.621	8.500	4.106	10.000	3.825	10.600	3.694	10.400	3.651
6.500	4.584	9.000	4.055	10.500	3.780	10.700	3.690	10.500	3.649
7.000	4.548	9.500	4.007	11.000	3.750	10.800	3.687	10.600	3.648
7.500	4.511	10.000	3.948	11.100	3.742	10.900	3.683	10.700	3.647
8.000	4.473	10.500	3.890	11.200	3.735	11.000	3.680	10.800	3.646
8.500	4.428	11.000	3.837	11.300	3.733	11.100	3.679	10.900	3.645
9.000	4.378	11.100	3.827	11.400	3.731	11.200	3.677	11.000	3.645
9.500	4.328	11.200	3.820	11.500	3.729	11.300	3.675	17.000	3.645
10.000	4.266	11.300	3.811	11.600	3.726	11.400	3.674		
10.200	4.238	11.400	3.806	11.700	3.724	11.500	3.673		
10.400	4.208	11.500	3.800	11.800	3.720	17.000	3.673		
10.600	4.176	11.600	3.796	11.900	3.719				
10.800	4.139	11.700	3.792	17.000	3.719				
11.000	4.100	11.800	3.789						
11.200	4.049	11.900	3.786						
11.400	4.007	12.000	3.784						
11.600	3.965	12.200	3.781						
11.800	3.927	12.400	3.779						
12.000	3.895	17.000	3.779						
12.200	3.867								
12.300	3.858								
12.400	3.856								
12.600	3.854								
17.000	3.854								

TABLE 1 (CONT'D)

SWEPT-LIP COWL INLET COORDINATES

PLANE F		PLANE G	
X	Y	X	Y
6.330	3.864	6.425	3.840
7.000	3.834	7.000	3.810
7.500	3.806	7.500	3.781
8.000	3.772	8.000	3.746
8.500	3.736	8.500	3.712
9.000	3.693	9.000	3.675
9.500	3.655	9.500	3.644
9.600	3.649	9.600	3.639
9.700	3.642	9.700	3.634
9.800	3.638	9.800	3.630
9.900	3.634	9.900	3.627
10.000	3.630	10.000	3.624
10.100	3.628	10.100	3.622
10.200	3.626	10.200	3.620
10.300	3.623	10.300	3.618
10.400	3.621	10.400	3.617
10.500	3.619	10.500	3.616
17.000	3.619	17.000	3.616